

# A temporal study of oxygen-rich pulsating variable AGB star, T Cep: Investigation on dust formation and dust properties

Suklima Guha Niyogi<sup>1</sup>, Angela K. Speck<sup>1</sup> & Takashi Onaka<sup>2</sup>

sgz94@mail.missouri.edu

## ABSTRACT

Pulsation is believed to be the leading cause of dusty mass loss from Asymptotic Giant Branch (AGB) stars. We present a temporal study of T Cep, a long-period Mira variable, using seven *ISO* SWS spectra, covering a 16-month period over a single pulsation cycle. The observed spectral dust features change over the pulsation cycle of this Mira. In general, the overall apparent changes in spectral features can be attributed to changes in the dust temperature, resulting from the intrinsic pulsation cycle of the central star. However, not all feature changes are so easily explained. Based on direct comparison with laboratory spectra of several potential minerals, the dust is best explained by crystalline iron-rich silicates. These findings contradict the currently favored dust formation hypotheses.

*Subject headings:* stars: AGB and post-AGB — stars: individual (T Cep) — (stars:) circumstellar matter — (ISM:) dust, extinction — infrared: stars

## 1. Introduction

Low and intermediate mass stars ( $0.8\text{--}8\text{ M}_{\odot}$ ) are major contributors to galactic chemical evolution. During the asymptotic giant branch (AGB) phase of their evolution, these stars lose a significant fraction of their mass through slow, massive winds at a rate of  $10^{-8} < \dot{M} < 10^{-4}\text{ M}_{\odot}\text{ yr}^{-1}$  (van Loon et al. 2005). This mass loss occurs as a result of stellar pulsation (Habing 1996) followed by acceleration of dust grains by radiation pressure (e.g. Gehrz & Woolf 1971; Höfner et al. 2007). Pulsation levitates atmospheric gas from

---

<sup>1</sup>Department of Physics & Astronomy, University of Missouri, Columbia, MO 65211

<sup>2</sup>Department of Astronomy, Graduate School of Science, The University of Tokyo, Bunkyo-ku, Tokyo 113-0033, Japan

the stellar surface. Then, as the outflowing gas cools, dust can condense in the outflow and capture the momentum of the star’s luminosity. Given that pulsation drives mass loss and affects the temperature and density distribution in the outflowing material, the effect of pulsation should be manifested in the nature of the dust, forming in the circumstellar region.

The mineralogy (i.e. composition and lattice structure) of the dust grains is determined by both the prevalent chemistry, and the physical characteristics (temperature and density distribution) of the outflowing gas. In turn, the chemistry is determined largely by the C/O ratio, and to some extent by the elemental abundances in the stellar atmosphere (metallicity). Convection currents inside the star transport newly-formed elements (especially carbon) from the helium- and hydrogen-burning shells to the surface of the star. Since carbon monoxide (CO) is a very stable molecule and forms very easily in such stellar atmospheres, carbon and oxygen atoms combine into CO, leaving the more abundant element to dominate the chemistry. Stars start their lives with cosmic C/O  $\approx 0.4$  (Asplund et al. 2009) and thus have oxygen-rich chemistry. In some cases, the dredge-up of carbon is efficient enough to raise C/O ratio above unity making the star carbon-rich (e.g. Wood 1988). Consequently oxygen-rich AGB stars can have  $0.4 \lesssim \text{C/O} < 1$ .

In this paper, we investigate a single long-period Mira variable T Cep as a case study to determine how the mineralogy and morphology of circumstellar dust varies with the pulsation cycle of the central star. We present analyses of time-variations in the infrared spectra, and show how the spectral dust features change over the variability cycle of this Mira. In § 2 we discuss the history of silicate mineralogy; in § 3 we describe the observations of T Cep; in § 4 we describe our analyses of the dust features, while the results are given in § 5. In § 6, we investigate the mineralogy of the dust and how it varies with time as well as the effect of grain shapes in dust spectral features. The overall discussion is in § 7, and the summary and conclusions are given in § 8.

## 2. Previous studies: dust around oxygen-rich AGB stars

Dust is very important in many astrophysical environments. In particular, due to the interplay between dust and stellar photons in driving mass loss, it is necessary to understand the nature of the dust around O-rich AGB stars. Dust grains absorb starlight and reemit photons according to their temperature and optical properties, typically in infrared (IR) region. Composition, lattice structure, grain size, and morphology all affect the resulting IR spectrum, as do the temperature and density distribution in the dust shell. We can compare laboratory spectra of different dust species to astronomical observations in order to identify the dust species present in circumstellar envelopes.

## 2.1. Finding silicates

In the late 1960s, while investigating deviations of stellar energy distributions from blackbodies, Gillett et al. (1968) discovered a peak near  $10\,\mu\text{m}$  in the spectra of four late-type, evolved, variable stars. Shortly thereafter a  $10\,\mu\text{m}$  absorption feature was discovered in the interstellar medium (ISM; Knacke et al. 1969; Hackwell et al. 1970). Initially this feature was attributed to silicate minerals (Woolf & Ney 1969), based on spectra of mixtures of crystalline silicate species predicted to form by theoretical models (Gaustad 1963; Gilman 1969). However, the laboratory spectra of crystalline silicate minerals showed more structure within the feature than observed in the astronomical spectra (see Woolf 1973; Huffman & Stapp 1973). Subsequent comparison with natural glasses (obsidian and basaltic glass; from e.g. Pollack et al. 1973) and with artificially disordered silicates (Day 1979; Krätschmer & Huffman 1979) showed that “amorphous” silicate was a better candidate for the  $10\,\mu\text{m}$  feature than any crystalline silicate.

Since the “amorphous” silicate  $10\,\mu\text{m}$  feature was first observed, it has been found to be almost ubiquitous being found in observations of evolved stars (e.g. Speck et al. 2000; Casassus et al. 2001); many lines of sight through the interstellar medium in our own galaxy (e.g. Chiar et al. 2007); and in nearby and distant galaxies (e.g. Hao et al. 2005). Further spectroscopic observations of O-rich AGB stars have found that these objects show a diverse range of spectral features, which are interpreted in terms of dust condensation hypotheses (e.g. Little-Marenin et al. 1990; Sloan & Price 1995; Speck et al. 2000). In order to understand how IR dust spectra are classified and the features are interpreted we need to discuss the currently-favored dust formation hypotheses.

## 2.2. Dust condensation sequence

Three competing dust formation mechanisms have been considered for circumstellar environments: (1) thermodynamic equilibrium condensation (Lodders & Fegley 1999); (2) formation of chaotic solids in a supersaturated gas followed by annealing (Stencel et al. 1990); (3) formation of seed nuclei in a supersaturated gas, followed by mantle growth (Gail & Sedlmayr 1999). The latter should follow thermodynamic equilibrium as long as density is high enough for gas-grain reactions to occur. Several observational studies support this thermodynamic condensation sequence (Dijkstra et al. 2005; Blommaert et al. 2007), however, the interpretation of the observational data is, in part, dictated by the condensation sequence. In 2, chaotic grains form with the bulk composition of the gas, and then anneal if the temperature is high enough (Stencel et al. 1990).

The thermodynamic condensation sequence for a gas cooling down from a high temperature is shown in Figure 1 (following Tielens 1990; Grossman 1972). The condensation sequence starts with the formation of refractory oxides (e.g.  $\text{Al}_2\text{O}_3$ ) which, upon cooling, react with gaseous SiO, Ca and Mg to form spinel ( $\text{MgAl}_2\text{O}_4$ , not shown in the figure), then to melilite (ranging from gehlenite  $[\text{Ca}_2\text{Al}_2\text{SiO}_7]$  to åkermanite  $[\text{Ca}_2\text{MgSi}_2\text{O}_7]$ ) and then to diopside ( $\text{CaMgSi}_2\text{O}_6$ ). The conversion of diopside to anorthite ( $\text{CaAl}_2\text{Si}_2\text{O}_8$ ) involves a solid-solid reaction, and is therefore kinetically unlikely.

In this sequence, the more abundant Mg/Fe-rich silicates form as mantles on the more refractory grains. Because of the relative abundance of Mg and Fe when compared to Ca and Al, most of the silicon atoms condense as the Mg-rich end member of the olivine family (forsterite:  $\text{Mg}_2\text{SiO}_4$ ). As the gas cools, the gaseous SiO converts forsterite into the Mg-rich end member of the pyroxene family (enstatite:  $\text{MgSiO}_3$ ). Consequently, the  $\text{MgSiO}_3/\text{Mg}_2\text{SiO}_4$  ratio increases with the decreasing temperature. At the pressure relevant for stellar outflows, gaseous Fe, may react with enstatite to form olivine with some iron ( $[\text{Mg}, \text{Fe}]_2\text{SiO}_4$ ). It is also predicted that Fe condense into metallic iron grains, but it is not predicted that the Fe-rich end members of the olivine (fayalite:  $\text{Fe}_2\text{SiO}_4$ ) or pyroxene series (ferrosilite:  $\text{FeSiO}_3$ ) will form. Regardless of the precise mineral into which it condenses, iron is expected to be in solid phase because it is strongly depleted from the gas phase (Okada et al. 2009).

Stellar winds are commonly assumed to be dust-driven in circumstellar environments of evolved stars (Ferrarotti & Gail 2006). Opacity of dusty materials is an important parameter for the wind-driving mechanism. If iron is absent from dust, a stellar wind cannot be driven because of the transparency of Mg-rich silicates. Iron has often been included in dust grains in order to increase the near-IR absorption efficiency (Tielens et al. 1998). However, the precise effect of the iron depends on how it is incorporated, i.e. as an integral part of the silicate (e.g. in amorphous  $[\text{Mg}, \text{Fe}]_2\text{SiO}_4$  silicate) or as metallic inclusions. For Mg-rich silicates with metallic iron inclusions, their absorption efficiency is so high that radiative heating leads to grain evaporation and only a limited amount of dust can survive (Woitke 2006).

For solar metallicity, Mg and Fe are approximately equally abundant in O-rich circumstellar environment (Lodders & Fegley 1999). In these dust condensation sequences, the condensation temperatures are dependent on the gas pressure. However, for the pressures relevant to the typical AGB outflow, the silicate formation temperatures are above the assumed glass transition temperature of 1000 K, implying that crystalline dust should form.

### 2.3. Spectral classification based on dust features

Various attempts have been made to classify the observed dust features of O-rich evolved stars (e.g. Little-Marenin et al. 1990; Sloan & Price 1995; Speck et al. 2000). All these authors have classified the observed spectra into groups according to the shape of the dust feature, which reflects a progression from a broad 9–12  $\mu\text{m}$  feature to the classic narrow 10  $\mu\text{m}$  silicate feature. This progression of the spectral features is expected to represent the evolution of the dust from the early forming refractory amorphous oxides (the broad feature) to the dominance of magnesium-rich amorphous silicates (the narrow 10  $\mu\text{m}$  feature) as described in § 2.2.

The most recent version of IR spectral class based on silicate emission is given by Sloan et al. (2003). They classify the silicate dust sequence by taking the flux ratios at 10, 11 and 12  $\mu\text{m}$ . They divided the sequence into eight segments, labeled SE1–SE8 (SE = silicate emission). Classes SE1–SE3 are expected to correspond to low-contrast alumina-rich amorphous dust seen in evolved stars losing mass at low rates and have optically thinner shells. Moving up the sequence, classes SE3–SE6 show structured silicate emission, with features at 10 and 11  $\mu\text{m}$ . The upper end of the silicate dust sequences (SE6–SE8) consist of sources with the classic silicate emission feature believed to be produced by amorphous silicate grains. These sources have optically thicker shells and higher mass-loss rates than sources at the other end of the sequence.

In addition to the SE# classification, based on the features in the 9–12  $\mu\text{m}$  range, another mid-IR feature at  $\sim 13 \mu\text{m}$  is sometimes present. Approximately 50% of O-rich AGB stars exhibit this feature and it has caused some controversy. The so-called “13  $\mu\text{m}$  feature” was discovered in the *IRAS* LRS spectra (Vardya et al. 1986) and does not lend itself to the standard IR feature classification system. It has been found in all SE classes (Speck et al. 2000; Sloan et al. 2003). Furthermore, the 13  $\mu\text{m}$  feature is associated with semiregular variables (SRs) rather than Miras or red supergiants (Sloan, LeVan & Little-Marenin 1996; Speck et al. 2000). Many minerals have been proposed by various authors (e.g. Sloan et al. 2003; DePew et al. 2006) as the likely carrier of this feature, including corundum (crystalline form of  $\text{Al}_2\text{O}_3$ ), spinel ( $\text{MgAl}_2\text{O}_4$ ) and silica ( $\text{SiO}_2$ ). Both corundum and spinel are a predicted condensates, presolar examples of which have been found in meteorites (e.g. Clayton & Nittler 2004, and references therein). However, spinel has been ruled out as the carrier of the 13  $\mu\text{m}$  feature because it also shows a strong feature at 17  $\mu\text{m}$  (irrespective of relative abundance of spinel), and this feature does not occur in the spectra of AGB stars that exhibit the 13  $\mu\text{m}$  (e.g. Sloan et al. 2003; Heras & Hony 2005; DePew et al. 2006). Furthermore, DePew et al. (2006) showed that only spherical grains of spinel or corundum give rise to a narrow 13  $\mu\text{m}$  feature; other grain shape distributions exhibit broader features at

longer wavelengths.

One of the most exciting recent findings in cosmic dust studies was the discovery of crystalline silicate dust by the Infrared Space Observatory (*ISO*; Kessler et al. 1996) Short Wavelength Spectrometer (SWS; de Graauw et al. 1996). Since then, crystalline silicates have been found in many astrophysical environments including the solar system and extra-solar planetary systems (e.g. Crovisier et al. 1996; Mann et al. 2006, and references therein), the circumstellar regions of both young stellar objects (Waelkens et al. 1996), and evolved stars (Waters et al. 1996; Molster et al. 2002a), and in other galaxies (Spoon et al. 2006). These crystalline silicates were first observed around evolved stars with very high mass-loss rates, leading to the inference that crystal formation requires such conditions (e.g. Cami et al. 1998). However, recent studies on occurrence of crystalline silicates and their distribution with evolution suggest that crystalline silicates preferentially occur around less-evolved, low mass-loss rate evolved stars (e.g. Sloan et al. 2010; McDonald et al. 2011).

The classical amorphous silicates have broad, smooth spectral features at  $\sim 10$  and  $18\ \mu\text{m}$ , with no diagnostic features at longer wavelengths; that is not true for crystalline silicates. A crystalline mineralogy would manifest itself more clearly at long IR wavelengths. Molster et al. (2002a,b,c) in their series of three papers studied dust mineralogy of several oxygen-rich (post-)AGB stars using *ISO* SWS data. By comparing the observational spectra with laboratory data, these authors concluded presence of Mg-rich crystalline silicates (both olivines and pyroxenes). However, the carrier of two of the observed far-IR features at  $\sim 20$  and  $32\ \mu\text{m}$ , need re-investigation.

Various authors (e.g. Begemann et al. 1996, and references therein) pointed to some connection between iron-rich (and possibly Mg-rich) oxide and an excess emission in the  $19\text{--}20\ \mu\text{m}$  range. Shortly thereafter, the  $19.5\ \mu\text{m}$  feature was attributed to  $\text{Mg}_{0.1}\text{Fe}_{0.9}\text{O}$  independently by Posch et al. (2002) and Cami (2003). Following this study, Lebzelter et. al. (2006) also attributed the same mineral for  $20\ \mu\text{m}$  feature, while studying the mid-IR dust features of AGB stars in the globular clusters 47 Tuc. However, the occurrence of circumstellar  $\text{Mg}_{0.1}\text{Fe}_{0.9}\text{O}$  is not expected from thermodynamic models (e.g. Lodders & Fegley 1999) and the low stability temperature of Mg-Fe oxides suggests that these minerals should not form directly from the gas phase. Consequently a large abundance of  $\text{Mg}_{0.1}\text{Fe}_{0.9}\text{O}$  is unlikely. Confirmation of this attribution is further hampered by the fact that Mg-Fe oxides exhibit only one resonance vibrational band in the IR region, which precludes verification of this composition by matching further features. A recent *Spitzer Space Telescope* (Werner et al. 2004) Infrared Spectrograph (IRS; Houck et al. 2004) study on globular cluster evolved stars also suggested that FeO is a good candidate for this  $\sim 20\ \mu\text{m}$  feature (McDonald et al. 2010). In addition their modeling suggests that metallic iron grains are present around O-rich AGB

stars, where it is observationally manifested as a featureless mid-IR excess.

Another interesting far-IR feature at  $\sim 32\mu\text{m}$  was studied by Molster (2000), and tentatively attributed to crystalline diopside ( $\text{CaMgSi}_2\text{O}_6$ , a pyroxene). Two recent independent studies of the spectrum of the AGB star RX Lac, attribute the  $\sim 32\mu\text{m}$  feature to two different minerals: diopside (Hony et al. 2009) and fayalite (Pitman et al. 2010). Diopside exhibits a prominent “ $25\mu\text{m}$  feature” which is absent in the spectrum of RX Lac, whereas, all fayalite spectral features are present. Pitman et al. (2010) studied the dust features of 4 O-rich AGB stars from SE1 class (RX Lac, T Cep, T Cet, R Hya) using *ISO* SWS data. Using new laboratory data for crystalline olivines, they showed that the spectral features for  $\text{Mg}_2\text{SiO}_4$  are not present in the observed spectra. Rather the authors found that the peak positions and widths of the spectral features of these 4 stars match better with non-endmember iron-rich silicate ( $\text{Mg}_{0.18}\text{Fe}_{1.82}\text{SiO}_4$ ). The authors concluded that this result is unexpected, but not entirely out of the question, since it has been long assumed that silicates in space include iron in order to account for their opacities. Moreover, Tielens et al. (1998) found iron-bearing dust to be more refractory than typical silicates, and therefore more likely to survive, which may explain the Pitman et al. (2010) result. In addition to these spectroscopic studies, recent work on presolar silicate grains from meteorites also suggests that there is more iron in silicate grains around AGB stars, than our current models allow (e.g. Stroud et al. 2008; Bose et al. 2010).

### 3. Observations of T Cep

The O-rich AGB star T Cep, was discovered by Ceraski in 1878, has been classified as spectral type M5.5e - M8.8e (Onaka et al. 1999) and infrared spectral class of SE1 (i.e. low-contrast broad dust feature/low mass-loss rate) with a  $13\mu\text{m}$  feature (Sloan et al. 2003). Its estimated distance is 210 pc from the HIPPARCOS catalogue (Perryman et al. 1997).

T Cep was observed using *ISO* SWS for seven times in a 16-month period (from August 1996 to December 1997) covering one full stellar variability period. The fully processed post-pipeline spectral data were acquired from an online atlas associated with Sloan et al. (2003). Detailed data reduction information is available from the atlas webpages<sup>1</sup>. Dates of the observations and TDT numbers are listed in Table 1, and all seven flux-calibrated spectra are shown in Figure 2 (seven observations are designated by sequential numbers).

In addition to the IR spectral data, we have also acquired light curve data of T Cep

---

<sup>1</sup><http://isc.astro.cornell.edu/sloan/library/swsatlas/atlas.html>

from American Association of Variable Star Observers (AAVSO) database<sup>2</sup>, which is shown in Figure 3. The positions in the lightcurve at which *ISO* SWS data was taken, are indicated by dashed straight lines. The apparent visual magnitudes at each *ISO* SWS observation are listed in Table 1. According to these light curve data from AAVSO, the estimated pulsation period of T Cep is 388 days, but the period shows evidence of variation. Castelaz et al. (2000) reported the pulsation period is of 398 days, whereas, Weigelt et al. (2003) showed the period is of 382 days. These variation of mean pulsation period of T Cep is confirmed to be real by Isles & Saw (1989) and these authors also reported that T Cep vary slowly in amplitude over the time. Also, an unusual secondary variation in T Cep had been reported by Marsakova & Andronov (2000), using the observation from AFOEV<sup>3</sup> and VSOLJ<sup>4</sup> databases (Schweitzer 1990; Nogami 1998), obtained over 75-years. These authors also reported significant variation of amplitude and asymmetry over the pulsation cycle, and they indicated the possibility of interference of pulsations with two periods to explain this unusual variation. Similar findings for other several long period Mira variables are also reported by several authors (e.g. Wood & Zarro 1981; Zijlstra & Bedding 2002; Benitez & Vargas 2002; Zijlstra et al. 2004).

#### 4. Analysing the dust spectral features of T Cep

In order to investigate the potential effects of the pulsation cycle on dust formation, we need to consider what contributes to the observed spectra. The spectrum,  $F_\lambda$ , can be interpreted as a product of the underlying continuum and an extinction efficiency factor ( $Q_\lambda$ ) for the entire spectrum,

$$F_\lambda = C \times Q_\lambda \times B_\lambda(T) \quad (1)$$

where  $B_\lambda(T)$  is the Planck function for a black body of temperature  $T$ ,  $Q_\lambda$  is a composite value including contributions from all dust grains of various sizes, shapes, crystallinities and compositions, and  $C$  is a scale factor that depends on the number of dust particles, their geometric cross section and the distance to the star. In reality the spectrum should be represented by:

---

<sup>2</sup><http://www.aavso.org/>

<sup>3</sup><ftp://cdsarc.u-strasbg.fr/pub/afoev>

<sup>4</sup><http://www.kusastro.kyoto-u.ac.jp>



$$F_\lambda = \sum_{i=1, j=1}^{n, m} C_j \times Q_{\lambda, j} \times B_{\lambda, i}(T_i) = \sum_{i=1, j=1}^{n, m} C_j \times Q_j \times B_i \quad (2)$$

where each  $B_i$  represents a single dust (or stellar) temperature black body (of which there are  $n$  in total), each  $Q_j$  represents the extinction efficiency for a single grain type as defined by its size, shape, composition and crystal structure, and each  $C_j$  represents the scale factor for a single grain type (of which there are  $m$  in total).

For T Cep, which is a low mass-loss rate AGB star and exhibits low-contrast spectral features, the spectrum is dominated by stellar photons. Furthermore, since T Cep has an optically thin dust shell (see e.g. Onaka et al. 1999; Sloan et al. 2003), its dust spectrum should be dominated by the hottest and densest part of the dust shell, which is essentially the inner dust radius. Therefore we can simplify Eq. 2 as:

$$F_\lambda = B_{\text{stellar}}(\lambda, T) + B_{\text{dust}} Q_{\text{dust}} \quad (3)$$

where  $B_{\text{dust}}$  is the Planck curve for the inner dust temperature ( $T_{\text{dust}}$ ), and  $Q_{\text{dust}}$  is the emission efficiency for the innermost dust grains. This assumption is an approximation to the dust continuum, but the exact continuum does not significantly alter the subsequent analysis.

Following Eq. 3 we can subtract the stellar contribution as approximated by an appropriate blackbody, leaving only the contribution from the dust shell. The stellar spectral energy distribution (SED) is assumed to be reasonably well simulated by a blackbody in the 2500–3500 K range. The precise temperature used in our analysis, was estimated from the spectral type and its variability over time. For the spectral observation closest to maximum light (T Cep4; hereafter T Cep<sub>max</sub>), we use a temperature of 3347 K, determined from the spectral type of M5.5 (Perrin et al. 1998); similarly at minimum light (T Cep7; hereafter T Cep<sub>min</sub>) we used a temperature of 2566 K, determined from the spectral type of M8.8, by extrapolating the data from Perrin et al. (1998). For the intermediate observations we linearly interpolated between these minimum and maximum temperatures, relating to their apparent changes in visual magnitude. Table 1 lists the estimated stellar blackbody temperatures ( $T_{\text{eff}}$ ) for all the seven observations. Figure 2 includes the original *ISO* spectra (in solid lines) together with the assumed stellar blackbodies (in dashed lines) in logarithmic scale (normalized at  $3.0 \mu\text{m}$ , averaging over the range from  $2.98\text{--}3.02 \mu\text{m}$ )<sup>5</sup>.

---

<sup>5</sup>while there may be molecular spectral features due to water within this range, visual inspection of the

In reality, these spectra contain contributions of the stellar photosphere, the extended atmosphere, and the circumstellar dust shell. In particular, stellar atmospheric water ( $\text{H}_2\text{O}$ ) molecules are major absorbers in the near-and-mid-IR range. If the stellar emission is dominated by the (cooler) water layer ( $\sim 2000$  K), the temperatures estimated from spectral type are too high. However, we have repeated our analysis using stellar temperatures in range 2000–3500 K (including ignoring the variation with pulsation phases) and found that the effect on spectral feature position, strength ratios and fitted dust temperature is negligible.

Having subtracted the starlight from our spectra, we are left with the emission from dust (i.e.  $B_{\text{dust}}Q_{\text{dust}}$ ; Eq. 3), which still contains a temperature factor. Therefore, we have fitted each starlight-subtracted spectrum with a blackbody representative of the inner dust temperature ( $T_{\text{dust}}$ ). The estimated dust blackbody temperatures ( $T_{\text{dust}}$ ) are listed in Table 1 and dust blackbodies are shown in Figure 2 (in dotted lines), together with the observed spectra and stellar continua.

Dividing each starlight-subtracted spectrum by the best-fitted dust blackbody curve (normalized at  $10.0\,\mu\text{m}$ , averaging over the range from  $9.98$ – $10.02\,\mu\text{m}$ ) leaves only the intrinsic absorption/emission properties of the dust “ $Q_{\text{dust}}$ ” (shown in Figure 4), by assuming all dust species have the same blackbody temperature. In this case, we effectively construct a composite emission efficiency spectrum which can be compared directly with absorptivity or mass absorption coefficient measurements of minerals in the laboratory. Hereafter, we refer to the starlight-subtracted, dust-continuum-divided spectra as continuum-eliminated spectra for simplicity.

Since, T Cep has an optically thin dust shell and its dust spectrum is dominated by the innermost dust, we can apply this simple modeling method, rather than the more complex radiative transfer modeling method. Radiative transfer modeling is known to be degenerate because it actually models optical depth ( $\tau$ ), which convolves geometrical shell thickness, opacity and density. Furthermore, most radiative transfer models use optical constants ( $n$  &  $k$ ) from laboratory experiments (or, worse, artificially derived optical constants), which are then applied usually using Mie theory to calculate the opacities/absorption cross sections of spherical grains. Recent studies (see e.g. Min et al. 2003; DePew et al. 2006; Pitman et al. 2008; Corman 2010) show that the use of spherical grains leads to unrealistic spectral features and this problem will be discussed further in § 6.3. In addition, mineral data in the form of optical constants (complex refractive index,  $n$  &  $k$ ) only exist for a limited set of

---

spectra shows these to be negligible, and the averaging over a range of wavelengths mitigates any potential problem. Furthermore since we are simply scaling a blackbody whose temperature is determined independent of the spectrum, small errors in scaling factor do not effect our results.

compositions. Available complex refractive indices are limited to the end-members of the olivine series (forsterite, fayalite), and for pyroxenes the situation is worse (only enstatite is available). Consequently, using radiative transfer modeling we cannot explore the mineralogical parameter space so thoroughly. Although, our simple modeling approach does not account for different sizes, shapes and/or temperatures within the dust grain population (see Thompson et al. 2006, for more discussion), it does allow us to explore the mineralogical parameter space comprehensively.

## 5. Results from analysis of T Cep’s spectrum

Table 1 shows that our modeled inner dust temperature ( $T_{dust}$ ) changes with pulsation cycle of the star. This result is not dependent on the precise temperature of the subtracted stellar black body. It is unexpected because it is usually assumed that dust forms at minimum light and the dust formation temperature is rather constant. However, the temperature at which dust can be formed depends on the mass-loss rate, which should vary through the stellar pulsation cycle. Thus the changing inner dust temperature may reflect the stability temperature at that moment in the pulsation cycle. Consequently, our simple model suggests that dust may not be formed constantly; rather it is sporadic. This finding is similar to that for another M-type variable star Z Cyg (Onaka et al. 2002).

We have calculated the linear correlation coefficients between the estimated stellar temperature ( $T_{eff}$ , which is derived from the visual magnitude and is thus a measure of the phase of pulsation) and the fitted dust temperature ( $T_{dust}$ ). There is a strong correlation<sup>6</sup> between them as shown in Figure 5, suggesting that the apparent change in dust temperature is dictated by the stellar variations, rather than the dust formation. This variation in inner dust temperature will be discussed further in § 6.2.

In order to study the dust properties (e.g. grain mineralogy, morphology) of T Cep, we concentrate on the continuum-eliminated spectra for the entire 8–45  $\mu\text{m}$ , all seven of which are shown in Figure 6: top panel. Since, the effect of dust temperature has been removed in our analysis (as discussed in § 4), there is no apparent change in overall underlying slope over the course of the pulsation period. However, in all cases there are clear spectral features that peak at 9.7, 11.3, 13.1, 20 and 32  $\mu\text{m}$ , indicated by dashed straight lines (see Figure 6: top panel). The sub-peak features within the broad 8–14  $\mu\text{m}$  complex emission features (at 9.7, 11.3, 13.1  $\mu\text{m}$ ) are explicitly shown in Figure 6: bottom panel. These sub-peak features

---

<sup>6</sup>The linear regression coefficient is  $R$ , but using the determination coefficient,  $R^2 > 0.5$  is a better criterion for whether a correlation exists (Thompson et al. 2006; Chan & Speck 2011)

are subtle, but we are confident that they are real because they do not occur at any known artifact wavelength of the SWS according to the SWS handbook<sup>7</sup>.

Previous studies of the *ISO* SWS spectra of T Cep discovered sharp molecular bands at 2.5, 7.3, 16.2  $\mu\text{m}$ , which are attributed to molecular  $\text{H}_2\text{O}$ ,  $\text{SO}_2$  and  $\text{CO}_2$  gas, respectively (e.g. Yamamura et al. 1999; Cami et al. 1999; Matsuura et al. 2002; Van Malderen 2003). The attribution of the 7.3  $\mu\text{m}$  feature has been further refined to be a combination of  $\text{H}_2\text{O}$  emission and  $\text{SiO}$  absorption (Verhoelst et al. 2006). Figure 2 shows that these molecular emission features change substantially with the pulsation cycle of T Cep, whereas the dust production shows only slight change. Molecular emission is affected more strongly than the dust emission by the stellar temperature, which changes with the pulsation cycle. The SpectraFactory database (Cami et al. 2010) shows that molecular  $\text{H}_2\text{O}$  and  $\text{OH}$  exhibit several spectral bands at  $\lambda > 20 \mu\text{m}$ . However, the molecular features are beyond the scope of the present work.

In addition to studying the molecular features, Van Malderen (2003) also studied the dust features of T Cep, using the same *ISO* SWS spectra presented here. He concurred that the dust spectra of T Cep are characterized by 9.7, 11, 13 and 19.5  $\mu\text{m}$  features, but his interpretation of the carriers of these features is different from our present analysis; he used amorphous silicate ( $\text{MgSiO}_3$ ), amorphous alumina ( $\text{Al}_2\text{O}_3$ ), spinel ( $\text{MgAl}_2\text{O}_4$ ) and amorphous magnesium-iron oxides ( $\text{Mg}_{0.1}\text{Fe}_{0.9}\text{O}$ ) respectively. However, as discussed in § 2.3, spinel is no longer considered the likely carrier of the 13  $\mu\text{m}$  feature, while  $\text{Mg}_{0.1}\text{Fe}_{0.9}\text{O}$  as the carrier of the 19.5  $\mu\text{m}$  feature also has some difficulties. Furthermore, using the same optical constants (see Table 2) used by Van Malderen, it is not possible to produce sharp enough features to explain those observed in the spectrum of T Cep (see Figure 7).

In order to understand the lattice structure and the mineralogy of the dust around T Cep, we have sought linear correlations amongst five prominent spectral features at 9.7, 11.3, 13.1, 20 and 32  $\mu\text{m}$ . To ensure that the measure of relative strength of the features is independent of the choice of continuum fitting technique, we define the relative intensity as the ratio of the flux measured at a peak position ( $F_{\text{peak}}(\lambda_1)$ ) to that measured at a continuum point ( $F_{\text{cont.}}(\lambda_2)$ ). In particular the relative intensity ( $F_{\text{peak}}(\lambda_1)/F_{\text{cont.}}(\lambda_2)$ ) is less likely to be affected by overlapping molecular absorption bands than any fitted continuum (especially from  $\text{SiO}$  absorption; Tsuji et al. 1997; Speck et al. 2000). The peak flux intensities are measured at  $\lambda_1 = 9.7, 11.3, 13.1, 20, 32 \mu\text{m}$  from each original flux-calibrated spectra. We used two separate continuum points (at  $\lambda_2 = 8.2$  and 40  $\mu\text{m}$ ) to verify our results. Towards the long wavelength end of the spectra the signal-to-noise deteriorates. The increased noise

---

<sup>7</sup>[http://iso.esac.esa.int/manuals/HANDBOOK/sws\\_hb/](http://iso.esac.esa.int/manuals/HANDBOOK/sws_hb/)

could affect our correlations. Consequently, we take the average flux in a wavelength bin covering the range of 39.9–40.1  $\mu\text{m}$  which contains 20 points.

Table 3 lists the determination coefficients ( $R^2$ ) for the flux ratios at peak positions ( $\lambda_1 = 9.7, 11.3, 13.1, 20, 32 \mu\text{m}$ ) with respect to the continuum points at ( $\lambda_2 = 8.2 \mu\text{m}$  and  $40 \mu\text{m}$ ). This table shows that not all the features have strengths which are strongly/significantly correlated if the continuum reference is at  $8.2 \mu\text{m}$ . However, if the reference continuum point of  $40 \mu\text{m}$  is used, almost all of the features have strongly/significantly correlated strengths. The discrepancy between these results for the different continuum points can be explained by the effect of SiO molecular absorption band, which may overlap with the  $8.2 \mu\text{m}$  region and make this wavelength point not truly continuum. If the SiO absorption is very strong, then the FWHM of the feature will be affected, but not necessarily the peak positions.

The strong correlations amongst all the peak features with respect to the  $40 \mu\text{m}$  continuum point (see Table 3) demonstrate that the  $32 \mu\text{m}$  is a real feature (as also discussed in § 2.3), rather than an artifact in these spectra, as suggested by Sloan et al. (2003). The strong correlation between  $9.7$  and  $11.3 \mu\text{m}$  features strongly suggests that the carrier is a crystalline olivine, rather than a combination of two separate minerals (i.e. amorphous silicate and amorphous alumina, as suggested by Van Malderen (2003)). Furthermore the strong correlations between the  $9$ – $12 \mu\text{m}$  complex features and the far-IR features at ( $20$  and  $32 \mu\text{m}$ ) provide evidence that these far-IR features probably arise from the same carrier (i.e. crystalline olivine). Moreover, some previous studies suggest the  $13 \mu\text{m}$  feature is carried by a different dust species from the rest of the “broad” feature (as discussed in § 2.3), the correlation of the  $13 \mu\text{m}$  feature with the numerous other features supports the hypothesis that this feature is due to some form of silicate (see Begemann et al. 1997; Speck et al. 2000). This will be further discussed in § 6.1. The positions of the spectral features and correlations amongst all these features together, suggests a crystalline silicate origin.

Having determined that the apparent broad spectral feature appears to be composed of overlapping features at  $9.7, 11.3, 13.1, 20, 32 \mu\text{m}$ , we must now consider the implications for the mineralogy of the dust around T Cep.

## 6. Mineralogy and morphology of dust grains around T Cep

### 6.1. Comparing T Cep spectrum with laboratory data of crystalline silicates

As discussed above, the *ISO* SWS spectra of T Cep, a low mass-loss rate O-rich AGB star, provide the evidence of crystalline silicates in its circumstellar environment, which call the current dust condensation sequences into question. From the strong correlations

among the spectral features (as discussed in § 5) the features at 9.7, 11.3, 20 and 32  $\mu\text{m}$  may be indicative of crystalline silicate minerals (as also mentioned by the following authors; Waters et al. 1996; Molster et al. 2002a; Pitman et al. 2010). While the correlations discussed in § 5 suggest that the carrier of the 13  $\mu\text{m}$  feature is a silicate, we do not have an exhaustive database of silicate mineral spectra to investigate this idea. In fact, silica-rich minerals can show a 13  $\mu\text{m}$  feature and future work to find spectra of silica-rich minerals may be fruitful. Meanwhile, whereas the 20  $\mu\text{m}$  feature has been attributed to  $\text{Mg}_{0.1}\text{Fe}_{0.9}\text{O}$  (e.g. Posch et al. 2002; Cami 2003), our analysis suggests a silicate origin because of the correlations amongst the features.

In order to match and identify the dust species present in the circumstellar envelope of T Cep, we compare the spectral features of the laboratory data from Pitman et al. (2010) and Hofmeister & Pitman (2007) (hereafter WashU Group) of different crystalline dust species to the *ISO* spectra of T Cep. In Figure 8, we compare the continuum-eliminated spectra of T Cep<sub>max</sub> and T Cep<sub>min</sub> with the laboratory absorptivity data for a selection of crystalline olivine samples of varying composition (data taken from Pitman et al. (2010)). Likewise, Figure 9 compares the same two T Cep spectra together with laboratory absorptivity data for a selection of crystalline pyroxene samples of varying composition (data taken from Hofmeister et al. in prep.)<sup>8</sup>

For the olivine data, FoX is an indication of the composition such that each olivine has the composition  $\text{Mg}_{2X/100}\text{Fe}_{2-2(X/100)}\text{SiO}_4$  (dataset ranging from Fo9 to Fo100 are shown in Figure 8); for the pyroxene data, EnX gives the composition via  $\text{Mg}_{X/100}\text{Fe}_{1-(X/100)}\text{SiO}_3$  (dataset ranging from En1 to En99 are shown in Figure 9). Since we have compiled laboratory mineral spectral data from a number of sources, these sources, along with other relevant sample/experimental information are listed in Table 2. The WashU laboratory spectra are in the form of absorbance ( $a$ ), which is proportional to the optical depth, whereas we need to compare to the absorption efficiency ( $Q_{\text{abs}}$ ). In order to convert the laboratory data to an appropriate form we use absorbance ( $a$ ) is proportional to the log of the absorptivity ( $A$ ), i.e.  $a \propto \ln(A)$ .

In general, we compare the spectral features of the laboratory spectra of different dust species to the astronomical observational data in order to match and identify the dust species present in circumstellar envelopes. However, the spectral feature parameters (po-

---

<sup>8</sup>We have a longstanding collaboration with Anne Hofmeister at WashU and can access new laboratory data through: <http://galena.wustl.edu/~dustspec/info.html>, even before publication. These crystalline olivine and pyroxene series spectra agree well with the laboratory data from Kyoto group (e.g. Koike et al. 2003; Chihara et al. 2002) but provide fine grid spacing in composition space. Comparison among the data from several laboratory groups will be further discussed in § 6.3.

sitions, strengths and widths) are significantly influenced by three parameters (composition, temperature and grain shape of the dust grains). The effect of these three parameters are discussed below.

It is clear from both Figures 8 (for the olivine family members) and 9 (for the pyroxene family members) that positions and strengths of the spectral features change with varying  $\text{Fe}/[\text{Mg}+\text{Fe}]$  ratio. The positions of peak features shift towards longer wavelength as the  $\text{Fe}/[\text{Mg}+\text{Fe}]$  ratio increases. For T Cep, the spectral features are more closely matched to Fe-rich silicate dust (Fo9 and En1), rather than expected Mg-rich silicate dust (Fo100 or En99; see Figure 8 and 9), which calls the conventional wisdom regarding the dust condensation sequence into question. These laboratory data compared to the observational spectra of T Cep, preclude the possibility of large abundances of the conventional Mg-rich silicates (Fo100, En99) to explain the dust features, unless grain shape or temperature effects can be invoked.

Koike et al. (2006) performed laboratory experiments to determine the effect of temperature on crystalline olivines. In general increasing temperature moves spectral features redwards as well as broadening and diminishing the heights of the features. This effect is most marked for far-IR features (at 49 and 69  $\mu\text{m}$  for forsterite), and is much less effective in the mid-IR (8–45  $\mu\text{m}$ ) region. The experiments covered a wide range of sub-room temperatures (8–292 K), and even this large change in temperature has little effect on the mid-IR features. Consequently, extrapolation of the effects to higher temperature still suggests that temperature is an insignificant factor in determining the positions of the spectral features with which we are concerned.

The third parameter often invoked to shift spectral features is grain shape (see e.g. Fabian et al. 2001; DePew et al. 2006; Sloan et al. 2006). This will be discussed in detail in § 6.3.

## 6.2. Investigation of mineralogy of dust around T Cep: Compositional mixtures

It is clear from the qualitative comparisons in Figures 8 and 9 that Fe-rich crystalline silicates (Fo9, En1) are promising constituents for the dust around T Cep.

Figure 10 shows comparison of continuum-eliminated spectra of T Cep<sub>max</sub> and T Cep<sub>min</sub> with mixture of these potential Fe-rich crystalline silicates minerals in different ratios. To account for the 13  $\mu\text{m}$  feature, we have also included spherical corundum ( $\text{Al}_2\text{O}_3$ ) grains. We use this mineral simply to give a feature, and not because we necessarily believe the carrier

to be corundum. The source of the laboratory data of corundum (Cor) and its chemical composition are listed in Table 2.

The best fit models from our calculations are mixtures of crystalline fayalite (Fo9; not-quite-endmember of olivine family), ferrosilite (En1) and corundum (Cor) in varying proportion (with the error-bars of 10% for each constituent). Although the models are not a perfect fit, there appears to be a variation from T Cep<sub>max</sub> to T Cep<sub>min</sub>. This variation is best explained by changing the ratio of Fo9 to En1. This is demonstrated in Figure 10, which shows the best fit models with T Cep<sub>max</sub> and T Cep<sub>min</sub> along with the laboratory data of each constituent separately.

Because laboratory optical properties of solids are produced for a variety of applications, the various laboratory data are published in several different types of units (e.g. absorbance, mass absorption coefficient, complex refractive index etc.) Using the appropriate conversion factors, all are converted to absorptivity ( $A$ ) before attempting to make mixtures for spectral fitting.

For Fo9 and En1 the original spectra were in absorbance ( $a$ ) units (e.g. Hofmeister et al. in prep; Pitman et al. 2010), which were converted to absorptivity ( $A$ ), using  $A \propto e^a$ . And for Cor, we used the Min et al. (2003) method to calculate the absorption cross section ( $C_{abs}$ ) for spherical grains of size  $0.1 \mu\text{m}$  using its optical constants (data taken from Gervais 1991). Absorptivity ( $A$ ) is directly proportional to the absorption efficiency  $Q_{abs}$  of a grain, which, in turn, is directly proportional to the absorption cross section ( $C_{abs}$ ).

We use the following linear conversion equation to convert  $C_{abs}$  to  $A$  for corundum:

$$A = C_{abs} \times n \times d \quad (4)$$

where  $n$  is the number of particle per unit volume of the material used, and  $d$  is the path length. For thin film,  $d$  is taken as  $1 \mu\text{m}$ . And to calculate  $n$ , we use

$$n = \frac{\rho}{M_{mol} \times m_{H_2}} \quad (5)$$

where  $\rho$  is the density of corundum ( $4.02 \text{ gm/cm}^3$ ),  $m_{H_2}$  is  $1.672 \times 10^{-24} \text{ gm}$ . And  $M_{mol}$  for  $\text{Al}_2\text{O}_3$  is  $(27 \times 2 + 16 \times 3 = 102)$ . Using these values in Eq 5, we get  $n = 2.35 \times 10^{22} \text{ cm}^{-3}$ . Knowing  $C_{abs}$ ,  $n$  and  $d$ , we calculated  $A$  for  $\text{Al}_2\text{O}_3$  by using Eq 4.

Figure 10 demonstrates that these mixtures produce a reasonably good match to the detailed shape and as well as overall shape of the spectrum for both T Cep<sub>max</sub> and T Cep<sub>min</sub>. Consequently, we can conclude that the compositions of the individual dust constituents



remain the same in both spectra, while the relative amounts of these constituents may change, but are consistent with no variations at all. The spectra are consistent with a variation in the ratio of Fo9/En1 such that it is doubled at maximum light (T Cep<sub>max</sub>) and the ratio is halved at minimum light (T Cep<sub>min</sub>), while the relative abundance of Cor remains unchanged. This suggests that the olivine grains are slightly favored at maximum light.

The apparent subtle changes in mineralogy with pulsation cycle may be entirely due to statistical effects. However, in the classic condensation sequence (shown in Figure 1), Mg-rich olivine exists at higher temperatures than Mg-rich pyroxene. Furthermore the Mg-rich olivine reacts with SiO gas to form Mg-rich pyroxene. If a similar reactive process exists for the iron-rich endmembers, the occurrence of higher olivine/pyroxene compositions at maximum light, may be a temperature effect. In this case, the Fe-rich pyroxene (En1) is more easily destroyed than the Fe-rich olivine (Fo9) at maximum light; while at minimum light the reaction with SiO gas is promoted. Essentially, the change in stellar radiation field causes selective destruction/processing of the inner most grains.

From our analysis, the most striking result is that we need Fe-rich crystalline silicates in order to explain the spectral features. This result is unexpected, but supported by recent studies of silicate presolar grains from meteorites which show that silicate grains from AGB stars have nano-crystalline structures and some are very iron-rich, indicative of non-equilibrium formation processes (e.g. Stroud et al. 2008; Vollmer et al. 2008; Bose et al. 2010).

### 6.3. Investigation of morphology of dust around T Cep: Grain shape effects

Our analysis on dust compositions around T Cep strongly suggest that the crystalline silicates are almost completely Fe-rich, with little evidence of Mg-rich silicates. This result conflicts with both current dust formation hypotheses, and studies of cosmic crystalline silicates to date. However, as mentioned in § 6.1, it is possible that grain shape effects may allow Mg-rich silicates to match the positions and strengths of the observed dust features of T Cep. Previous studies show that the position of spectral features of dust grains depend on their grain shapes (see Bohren & Huffman 1983; Bohren et al. 1983; Fabian et al. 2001; Min et al. 2003; Sloan et al. 2006; DePew et al. 2006; Koike et al. 2010). Here we investigate the grain shape effects of crystalline silicates.

The spectral features of crystalline silicate grains exhibit wide variety in the positions, widths and strengths of their peaks. For a given series, these are dependent on the composition (Fe/[Mg+Fe] ratio) of the silicates, as well as the temperatures (as discussed in

§ 6.1) and shapes of dust grains. Disentangling these competing effects is difficult because we do not have the data to test both grain shape and compositional effects simultaneously. There are several laboratories that have produced spectral data for crystalline silicates in the olivine and pyroxene series. The three laboratories, which are most noted for these studies are WashU (e.g. Hofmeister & Pitman 2007; Pitman et al. 2010), Kyoto (e.g. Chihara et al. 2002; Koike et al. 2003, 2006; Murata et al. 2009; Koike et al. 2010) and Jena (e.g. Fabian et al. 2001; Jäger et al. 1998) groups.

A series of opacity (mass absorption coefficients) measurements for the olivine series, covering several Fe/[Mg+Fe] ratios from forsterite (Fo100) to fayalite (Fo0) has been published by the Kyoto group (Koike et al. 2003). A finer grid of compositions across the olivine series was published by the WashU group (Hofmeister & Pitman 2007; Pitman et al. 2010), which agree with the Kyoto data. Here we use to finer grid of Pitman et al. (2010). A similar series of measurements for pyroxene from enstatite (En100) to ferrosilite (En1) has been also published by the Kyoto group (Chihara et al. 2002). Here, we use currently unpublished pyroxene data from the WashU group (Hofmeister et al. in prep.), which also agree with the Kyoto data.

While the data from WashU and Kyoto groups provide a good sampling over several Fe/[Mg+Fe] ratios for both olivines and pyroxenes, they do not measure the complex indices of refraction or dielectric constants for all these compositions. As a consequence we cannot use them to analyze the effect of grain shape on dust spectra. Thus we cannot fit both the compositional effect (Fe/[Mg+Fe] ratio) and the shape distribution simultaneously. For this reason, extensive studies of grain shape effects have generally been limited to a single composition: forsterite (Fo100), supplied by the Jena group.

The complex refractive indices for the end-member compositions of olivine (Mg-rich olivine: Fo90<sup>9</sup>, fayalite: Fo0) and Mg-rich pyroxene (enstatite: En100) are provided by the Jena group<sup>10</sup> (e.g. Fabian et al. 2001; Jäger et al. 1998). The refractive indices are provided for the vibrational directions parallel to the three crystallographic axes  $x$ ,  $y$ ,  $z$ . Meanwhile, Mukai & Koike (1990) provided optical constants for forsterite (Fo100), but this data was for unoriented samples and therefore represents an average of the three axial directions. A list of all the sources of these laboratory data used, can be found in Table 2.

Since solid particles in astrophysical environments are expected to be very irregular in shape, it is very difficult to characterize the shape of the particles in a simple way.

---

<sup>9</sup>Technically Fo90 is still called forsterite and most natural samples are closer to Fo90 than Fo100

<sup>10</sup>optical constants available at <http://www.astro.uni-jena-de/Laboratory/Database/databases.html>

Traditionally, cosmic dust grains have been assumed to be spherical for simplicity, however, it is becoming increasingly obvious that the use of spherical grains leads to unrealistic spectral features (see e.g. Min et al. 2003; DePew et al. 2006; Pitman et al. 2008; Corman 2010). There are several possible approaches to addressing the grain shape effect, which we will compare here.

Fabian et al. (2001) used their optical constants of crystalline Mg-rich olivine (Fo90) and fayalite (Fo0) to calculate mass absorption coefficients for IR region for a variety of grain shapes. These authors primarily chose: spherical grains, ellipsoids elongated along the  $z$ -axis, and distributions of ellipsoids; based on the assumption that mineral forms crystalline ellipsoids elongated along the  $z$ -axis, when condensing from the gas phase at high temperature. Whether there should be a preferred growth axis for a grain shape or not, will be discussed below. These authors compared their calculated mass absorption coefficients data directly with *ISO* SWS observational data of evolved stars. They concluded that the spectral features are shifted in wavelength by grain shape effects and this effect is prominent in mid-IR region, whereas, the spectral features in far-IR region remain practically unaffected by the particle shape.

Recent experimental studies by Takigawa et al. (2009) on the evaporation of single crystals of forsterite (Fo100) show that this mineral evaporates anisotropically, which may lead to distinct grain shape distributions (e.g. disk-shaped dust grain, flattened along the  $y$  or  $z$  axes). They showed that forsterite always evaporates anisotropically, but the details of the anisotropy (i.e. which axis is elongated) depends on the experimental conditions (total gas pressure and temperature). They conclude that the precise shape of forsterite grains depends on the formation conditions in space. Because the peak positions and relative strengths of dust spectral features are expected to depend on grain shape, these spectral parameters may be diagnostic of the formation and heating conditions for the dust grains.

Another recent study by the Kyoto group investigated how the spectral features of forsterite (Fo100) are affected by grain shape (Koike et al. 2010). They measured the IR mass absorption coefficients of forsterite grains of a variety of shapes including irregular, plate-like with no sharp edges, elliptical, cauliflower and spherical. They concluded that spectral features of forsterite in mid-IR region (at 11, 19, 23, 33  $\mu\text{m}$ ) are extremely sensitive to particle shape, whereas, the features in far-IR region (at 49, 69  $\mu\text{m}$ ) remained unchanged despite of the different grain shapes (c.f. Fabian et al. 2001).

Min et al. (2003) adopted statistical approach (following Bohren & Huffman 1983) in order to understand the effect of grain shape on IR dust features of forsterite (Fo100). They considered the limiting case, where the particles are very small compared to the wavelength of radiation (Rayleigh domain). In this statistical approach, the scattering and absorption

properties of irregularly shaped particles can be simulated by the average properties of a distribution of simple shapes (such as ellipsoids, spheroids, and hollow spheres). They calculated the absorption and scattering cross sections of different grain shapes and concluded that there is a strong similarity between the absorption spectra of distributions of various non-spherical homogeneous particles (e.g. ellipsoid, spheroids) and a distribution of hollow spheres in Rayleigh domain, but that homogenous spherical particles show a markedly different spectrum.

Using the approach of Min et al. (2003) and assuming that there is no tendency for a certain axis to be elongated, we have calculated the absorption cross-sections ( $C_{\text{abs}}$ ) for three compositions of olivine (Fo100, Fo90 and Fo0; see Table 2 for sources of complex refractive indices). For each composition, we calculate  $C_{\text{abs}}$  for four grain shape distributions: Spherical particle (SPH), Continuous distribution of ellipsoids (CDE), Continuous distribution of spheroids (CDS), and Distribution of hollow spheres (DHS)<sup>11</sup>. The grain size is defined by the grain volume being equivalent to a sphere of radius  $0.1 \mu\text{m}$ . When data is available for the individual crystallographic axes, we calculate the  $C_{\text{abs}}$  separately and then average the three axial absorption cross sections ( $\langle C_{\text{abs}} \rangle$ ). The final  $\langle C_{\text{abs}} \rangle$  spectra are shown in Figures 11–15.

For all three compositions (Fo100, Fo90 and Fo0), the spectral feature parameters (e.g. peak positions and strengths) are similar for both ellipsoids (CDE) and spheroids (CDS). For the hollow spheres (DHS) the peak positions are similar to both CDE and CDS, but the spectral features are stronger. The spectral features of spherical (SPH) particles are significantly different in both position and strength from those of CDE, CDS and DHS.

Figure 15 compares the positions of the spectral features in the derived absorption cross-sections with those observed for T Cep. It is clear that fayalite (Fo0) provides a better match with the observed peak positions (at  $20, 32 \mu\text{m}$ ) of T Cep, than does forsterite (Fo100). Following the work of Takigawa et al. (2009), it is possible that a single growth axis is elongated. However, Figure 15 shows that even using only a single crystallographic axis does not produce an Mg-rich olivine with features that match T Cep.

## 7. Discussion

Our analysis of the spectra of T Cep strongly suggest that the dust forming around this Mira is both highly crystalline and iron-rich. This has implications for not only for other stars exhibiting these crystalline features, but also for conventionally Mg-rich condensation

---

<sup>11</sup>Hollow spheres are meant to simulate fluffy grains

sequence observed for amorphous circumstellar silicates.

Woitke (2006) showed that while carbon dust around an AGB star could drive a radiation-pressured wind, oxygen-rich dust (silicate) was too transparent. However, this result assumes the silicates are Mg-rich. Iron-rich silicate grains tend to have higher optical/near-IR opacities which facilitate the capture of momentum from the star through radiation pressure. The inclusion of iron-rich silicate grains may solve this problem.

Woitke (2006) also showed that the dynamics in the dust-forming zones around carbon-rich AGB stars lead to inhomogeneous dust formation, producing fine scale structure in the density of the dust envelope. In these models the only condensate considered is amorphous carbon. In an oxygen-rich environment, there are many potential minerals that can be formed and their stability is sensitive to the precise conditions. In addition to the turbulent/hydrodynamic density inhomogeneities predicted by Woitke (2006), pulsation shocks are expected to have a strong effects on local conditions (e.g. Cherchneff 2006). This combination of physical effects should lead to non-equilibrium dust formation and may lead to unexpected dust-forming conditions. Therefore we suggest that even at low mass-loss rates the density structure in the outflows of AGB stars is such that crystalline silicates may form, though it is not clear why iron-rich silicates are apparently favored.

## 8. Summary & Conclusion

We have presented an analysis of the time variations of the IR dust spectrum of optically thin O-rich AGB star, T Cep.

We found that:

1. The inner dust temperature of T Cep is variable.
2. Dust formation is likely to be sporadic, not continuous, and has approximately the same composition all the time.
3. While the observations are consistent with a constant olivine-to-pyroxene ratio, they can accommodate small variations with stellar pulsation. This variation in composition is very subtle and can be explained by selective destruction/processing of the inner most grains with the change in stellar radiation field.
4. The strong correlations between the observed spectral features suggest that they all have same crystalline mineral as a carrier.

5. The structure within the broad 8–14  $\mu\text{m}$  feature with overlapping sub-features at 9.7, 11.3, 13.1  $\mu\text{m}$  is explained by mixtures of crystalline silicates. This confirms the presence of crystalline minerals around low-mass-loss rate O-rich AGB stars.
6. The peak wavelength of the features at 20 and 32  $\mu\text{m}$  suggest the presence of Fe-rich, rather than the expected Mg-rich silicates. This can be explained as occurrence of non-equilibrium condensation mechanism in the outflow of the central star.

The analysis presented here shows that our understanding of the formation of crystalline silicates and the inclusion of iron in those silicates is in its infancy and needs to be revised according to the present findings.

Acknowledgements: We are grateful to the anonymous reviewers, whose comments significantly improved this paper. And we thank Dr. Catharinus Dijkstra for providing his code to calculate the absorption cross section for four different grain shapes of various minerals.

This work is supported by NSF CAREER AST-0642991.

## REFERENCES

- Asplund, M., Grevesse, N., Sauval, A. J., Scott, P., 2009, *ARA&A*, 47, 481.
- Begemann, B., Dorschner, J., Henning, Th., Mutschke, H. 1996, *ApJ*, 474, L195.
- Begemann, B., Dorschner, J., Henning, Th., Mutschke, H., Guertler, J., Koempe, C., Nass, R., 1997, *ApJ*, 476, 199.
- Benitez, P. M., Vargas, M. J., 2002, *JBAAA*, 112, p349.
- Blommaert, J. A. D. L., Vanhollebeke, E., Cami, J, et al., 2007, in *ASP Conf. Ser. 378, Why Galaxies Care About AGB Stars: Their Importance as Actors and Probes*, ed. F. Kerschbaum, C., p164.
- Bohren, C. F., Huffman, D. R., Kam, Z., 1983, *Nature*, 306, 625.
- Bohren, C. F., & Huffman, D. R., 1983, *Absorption and Scattering of Light by Small Particles* (John Wiley & Sons Inc., New York) 530.
- Bose, M., Floss, C., Stadermann, F. J., 2010, *ApJ*, 714, 1624.
- Cami, J., de Jong, T., Justtanont, K., Yamamura, I., Waters, L. B. F. M., 1998, *Ap&SS*, 255, 339.

- Cami, J., Yamamura, I., de Jong, T., Onaka, T., Tielens, A. G. G. M., Justtanont, K., Waters, L. B. F. M., 1999, *ESASP*, 427, 281.
- Cami, J., Mass-losing pulsating stars and their circumstellar matter. Workshop, May 13–16, 2002, 283, p209.
- Cami, J., van Malderen, R., Markwick, A. J., 2010, *ApJS*, 187, 409.
- Casassus, S., Roche, P. F., Aitken, D. K., Smith, C. H., 2001, *MNRAS*, 320, 424.
- Castelaz, M. W., Luttermoser, D. G., Caton, D. B., Piontek, R. A., 2000, *AJ*, 120, 2627.
- Chan, S.J., Speck, A.K., 2011 in review.
- Cherchneff, I., 2006, *A&A*, 456, 1001.
- Chiar, J. E., Tielens, A. G. G. M., 2006, *ApJ*, 637, 774.
- Chiar, J. E., Ennico, K., Pendleton, Y. J., et al., 2007, *ApJ*, 666, L73.
- Chihara, H., Koike, C., Tsuchiyama, A., 2007, *A&A*, 464, 229.
- Chihara, H., Koike et al., 2002, *A&A*, 391, 267.
- Clayton, D. D., Nittler, L. R., 2004, *ARA&A*, 42, 39.
- Corman, Adrian, 2010, Ph.D. Thesis, University of Missouri.
- Crovisier, J. et al., 1996, *A&A*, 315, L385.
- Day, K.L., 1979, *ApJ*, 234, 158.
- de Graauw, T., Haser, L. N., Beintema, D. A., et al., 1996, *A&A*, 315, L49.
- DePew, K., Speck, A., Dijkstra, C., 2006, *ApJ*, 640, 971.
- Dijkstra, C., Speck, A. K., Reid, R. B., Abraham, P., 2005, *ApJ*, 633, L133.
- Doyle, D., Pilbratt, G., Tauber, J., 2009, *Proceedings of the IEEE*, 97, p1403.
- Fabian, D., Henning, T., Jäger, C., Mustschke, H., Dorschner, J., Wehrhan, O. 2001, *A&A*, 378, 228.
- Ferrarotti, A. S., Gail, H.-P., 2006, *A&A*, 447, 553.
- Flower, P., 1996, *ApJ*, 469, 355.

- Gail, H.-P., Sedlmayr, E., 1999, *A&A*, 347, 594.
- Gaustad, J. E., 1963, *ApJ*, 138, 1050.
- Gehrz, R. D., Woolf, N. J., 1971, *ApJ*, 165, 285.
- Gervais, F., 1991, in *Handbook of Optical Constants of Solids*, 761.
- Gillett, F. C., Low, F. J., Stein, W. A., 1968, *ApJ*, 154, 677.
- Gilman, R.C., 1969, *ApJ*, 155, L185.
- Grossman, L., 1972, *Geochim. Cosmchim. Acta*, 36, 597.
- Habing, H. J., 1996, *A&ARv*, 7, 97.
- Hackwell, J. A., Gehrz, R. D., Woolf, N. J., 1970, *Nature*, 227, 822.
- Hao, L., Spoon, H. W. W., Sloan, G. C., et al., 2005, *ApJ*, 625, 75.
- Henning, T., Begemann, B., Mutschke, H., Dorschner, J., 1995, *A&A*, 112, 143.
- Heras, A. M., Hony, S., 2005, *A&A*, 439, 171.
- Hofmeister, A. M., Pitman, K. M., 2007, *Phys. Chem. Min*, 34, 319.
- Höfner S., Andersen A.C., 2007, *A&A*, 465, L39.
- Höfner S., 2008, *A&A*, 491, L1.
- Honda, M., Kataza, H., Okamoto, Y. K., Miyata, T., Yamashita, T., Sako, S., Takubo, S., Onaka, T., 2003, *ApJ*, 585, L59.
- Hony, S., Heras, A. M., Molster, F. J. and Smolders, K., 2009, *A&A*, 501, 609.
- Houck, J. R., Roellig, T. L., Van Cleve, J., Forrest, W. J., et al. 2004, in *Optical, Infrared, and Millimeter Space Telescopes*. Edited by Mather, John C. *Proceedings of the SPIE*, 5487, p.62.
- Huffman, D. R., Stapp, J. L., 1973, in *Interstellar Dust and Related Topics*. IAU Symp. 52, (Eds) J. Mayo Greenberg and H. C. van de Hulst. Dordrecht, Boston, Reidel, p.297.
- Isles, J. E., Saw, D. R. B., 1989, *JBAA*, 99, p.121.
- Jäger, C.; Mutschke, H., Begemann, B., Dorschner, J., Henning, Th., 1994, *A&A*, 292, 641.



- Jäger C., Molster, F. J., Dorschner, J., Henning, Th., Mutschke, H., Waters, L. B. F. M., 1998, *A&A*, 339, 904.
- Kessler, M. F., Steinz, J. A., Anderegg, M. E., 1996, *A&A*, 315, L27.
- Knacke, R. F., Gaustad, J. E., Gillett, F. C., Stein, W. A., 1969, *ApJ*, 155, L189.
- Koike, C., Chihara, H., Tsuchiyama, A., Suto, H., Sogawa, H., Okuda, H., 2003, *A&A*, 399, 1101.
- Koike, C., Mutschke, H., Suto, H., Naoi, T., Chihara, H., Henning, Th., Jäger, C., Tsuchiyama, A., Dorschner, J., Okuda, H., 2006, *A&A*, 449, 583.
- Koike, C., Imai, Y., Chihara, H., Suto, H., Murata, K., Tsuchiyama, A., Tachibana, S., Ohara, S., 2010, *ApJ*, 709, 983.
- Krätschmer, W., Huffman, D. R., 1979, *Ap&SS*, 61, 195.
- Lebzelter, Th., Posch, Th., Hinkle, K., Wood, P. R., Bouwman, J., 2006, *ApJ*, 653, L145.
- Little-Marenin, I. R., Little, S. J., 1990, *AJ*, 99, 1173.
- Lodders, K., Fegley, B., Jr., 1999, in *IAU Symp. 191, Asymptotic Giant Branch Stars*, ed. T. Le Bertre, A. Lebre, C. Waelkens (New York: Springer), 279.
- McDonald, I., Sloan, G. C., Zijlstra, A. A., Matsunaga, N., Matsuura, M., Kraemer, K. E., Bernard-Salas, J., Markwick, A. J., 2010, *ApJ*, 717, L92.
- Mann, I., Köhler, M., Kimura, H., Cechowski, A., Minato, T., 2006, *AJ*, 13, 159.
- Marsakova, V. I., Andronov, I. L., 2000, *The Impact of Large-Scale Surveys on Pulsating Star Research*, ASP Conference Series, 203, 131.
- Matsuura, M., Yamamura, I., Cami, J., Onaka, T., Murakami, H., 2002, *A&A*, 383, 972.
- McDonald, I., Boyer, M. L., van Loon, J. Th., Zijlstra, A. A., 2011, *ApJ*, arXiv:1101.1096.
- Min, M., Hovenier, J. W., de Koter, A., 2003, *A&A*, 404, 35.
- Molster, F. J., 2000, Ph.D. Thesis, University of Amsterdam.
- Molster, F. J., Waters, L. B. F. M., Tielens, A. G. G. M., Barlow, M. J., 2002, *A&A*, 382, 184.
- Molster, F. J., Waters, L. B. F. M., Tielens, A. G. G. M., 2002, *A&A*, 382, 222.

- Molster, F. J., Waters, L. B. F. M., Tielens, A. G. G. M., Koike, C., Chihara, H., 2002, *A&A*, 382, 241.
- Monnier, J. D., Geballe, T. R., Danchi, W. C., 1998, *ApJ*, 502, 833.
- Mukai, T., Koike, C., 1990, *Icarus*, 87, 180.
- Murata, K., Takakura, T., Chihara, H., Koike, C., Tsuchiyama, A., 2009, *ApJ*, 696, 1612.
- Murata, K., Chihara, H., Koike, C., Takakura, T., Imai, Y., Tsuchiyama, A., 2009, *ApJ*, 697, 836.
- Nogami, D., 1998, *Wild Stars In The Old West: Proceedings of the 13th North American Workshop on Cataclysmic Variables and Related Objects*. ASP Conference Series, 137, p.495.
- Okada, Y., Onaka, T., Kaneda, H., Sakon, I., 2009, *SPICA joint European/Japanese Workshop*. EDP Sciences, p.03008.
- Onaka, T., de Jong, T., Yamamura, I., Cami, J., Tanabé, T., 1999, *ESASP*, 427, 381.
- Onaka, T., de Jong, T., Yamamura, I., 2002, *A&A*, 388, 573.
- Perrin, G., Coude, du F., Ridgway, S. T., Mariotti, J.-M., Traub, W. A., Carleton, N. P., Lacasse, M. G., 1998, *ApJ*, 331, 619.
- Perryman, M. A. C., Lindegren, L., Kovalevsky, J., et al., 1997, *A&A*, 328, L49.
- Pitman, K. M., Hofmeister, A. M., Corman, A. B., & Speck, A. K. 2008, *A&A*, 483, 661.
- Pitman, K. M., Dijkstra, C., Hofmeister, A. M., Speck, A. K., 2010, *MNRAS*, 406, 460.
- Poglitsch, A., Waelkens, C., Geis, N., et al. 2010, *A&A*, 518, L2.
- Pollack, J. B., Toon, O. B., Khare, B. N., 1973, *Icarus*, 19, 372.
- Posch, Th., Kerschbaum, F., Mutschke, H., Dorschner, J., Jger, C., 2002, *A&A*, 393, L7.
- Schweitzer, E., 1990, *JAVSO*, 19, 122.
- Sloan, G. C., Price, S. D., 1995, *ApJ*, 451, 758.
- Sloan, G. C., Price, S. D., 1998, *ApJ*, 119, 141.
- Sloan, G. C., Levan, P. D., Little-Marenin, I. R., 1996 *ApJ*, 463, 310.

- Sloan, G. C., Kraemer, Kathleen E., Goebel, J. H., Price, S. D., 2003, *ApJ*, 594, 483.
- Sloan, G. C., Devost, D., Bernard-Salas, J., Wood, P. R., Houck, J. R., 2006 *ApJ*, 638, 472.
- Sloan, G. C., Matsunaga, N., Matsuura, M., Zijlstra, A. A., 2010, *ApJ*, 719, 1274.
- Speck, A. K., Barlow, M. J., Sylvester, R., J., Hofmeister, A. M., 2000, *A&A*, 146, 437.
- Spoon, H. W. W., et al., 2006, *ApJ*, 638, 759.
- Stencel, Robert E., Nuth, Joseph A., III, Little-Marenin, Irene R., Little, Stephen J., 1990, *ApJ*, 350, L45.
- Stroud, R. M., Nguyen, A. N., Alexander, C. M. O’d., Nittler, L. R., Stadermann, F. J., 2008, *Meteoritics & Planet. Sci. Abst.* 43, 5201.
- Takigawa, A., Tachibana, S., Nagahara, H., Ozawa, K., Yokoyama, M., 2009, *ApJ*, 707, 97.
- Thompson, G.D., Corman, A.B., Speck, A.K., Dijkstra, C. 2006, *ApJ*, 652, 1654.
- Tielens, A. G. G. M., 1990, in *From Miras to Planetary Nebulae: Which Path for Stellar Evolution*, ed. M. O. Mennessier A. Omont (Gif-sur-Yvette: Editions Frontieres), 186.
- Tielens, A. G. G. M., Waters, L. B. F. M., Molster, F. J., Justtanont, K., 1998, *Ap&SS*, 255, p.415–426.
- Tsuji T., Ohnaka K., Aoki W., Yamamura I., 1997, *A&A*320, L1.
- Vardya, M.S., de Jong, T., Willems, F.J., 1986, *ApJ*, 304, L29.
- van Loon, J. T., Cioni, M.-R. L., Zijlstra, A. A., Loup, C., 2005, *A&A*, 438, 273.
- Van Malderen, R., 2003, *On the analysis of the IR spectra of cool giants: model atmospheres and time-dependent behaviour*, Ph.D thesis, Katholieke Universiteit Leuven.
- Verhoelst, T., Decin, L., van Malderen, R., Hony, S., Cami, J., 2006, *A&A*, 447, 311.
- Vollmer, C., Hoppe, P., Brenker, Frank E., 2008, *ApJ*, 684, 611.
- Waelkens, C. et al., 1996, *A&A*, 315, L245.
- Waters, L. B. F. M., et al., 1996, *A&A*, 315, L361.
- Weigelt, G., Beckmann, U., Blöcker, T., Hofmann, K.-H. et al., 2003, *ANS*, 324.
- Werner, M. W., Roellig, T. L., Low, F. J., et al., 2004, *A&A*, 315, L27.

- Woitke, P., 2006, A&A, 452, 537.
- Woitke, P., 2006, A&A, 460, L9.
- Wood, P. R., 1988, LNP, 305, 31.
- Wood, P. R., Zarro, D. M., 1981, ApJ, 247, 247.
- Woolf, N. J., Ney, E. P., 1969, ApJ, 155, L181.
- Woolf, N. J., 1973, IAUS, 52, 485.
- Yamamura, I., de Jong, T., Onaka, T., Cami, J., Waters, L. B. F. M., 1999, A&A, 341, L9.
- Zijlstra, A. A., Bedding, T. R., 2002, JAVSO, 31, p.2.
- Zijlstra, A. A., Bedding, T. R., Markwick, A. J., Loidl-Gautschy, R., et al., 2004, MNRAS, 352, 325.

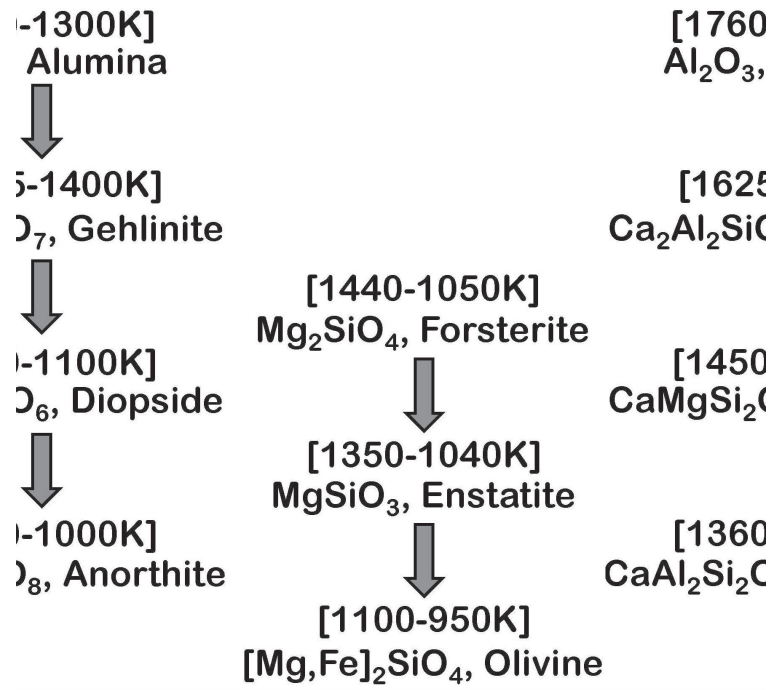


Fig. 1.— Predicted condensation sequence for O-rich environments from Tielens (1990) (after Grossman 1972).

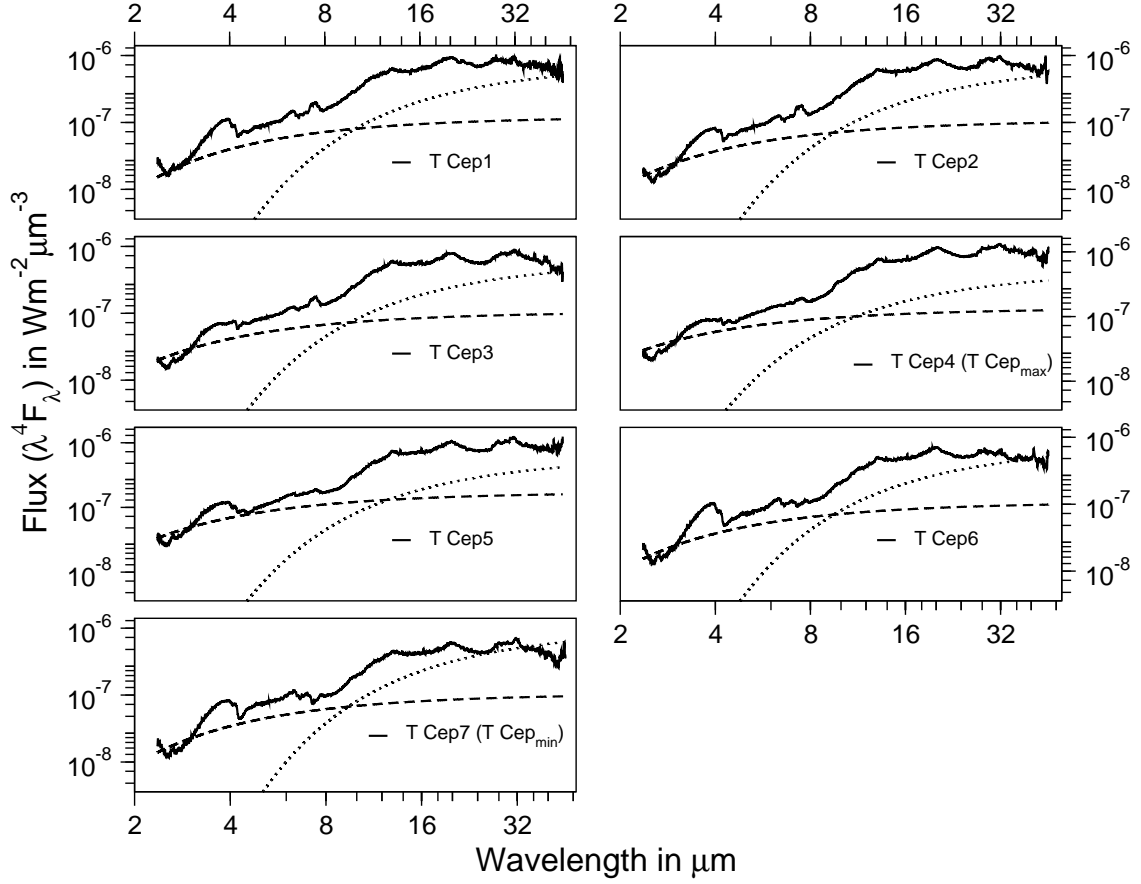


Fig. 2.— *ISO* SWS spectra of T Cep together with both stellar and dust continua. *solid lines* are the observed spectra; *dashed lines* are fitted stellar blackbody continua; *dotted lines* are dust blackbody continua (see text for details). The estimated temperatures of the stellar blackbodies ( $T_{\text{eff}}$ ) and the fitted temperatures for the dust blackbodies ( $T_{\text{dust}}$ ) are listed in Table 1.

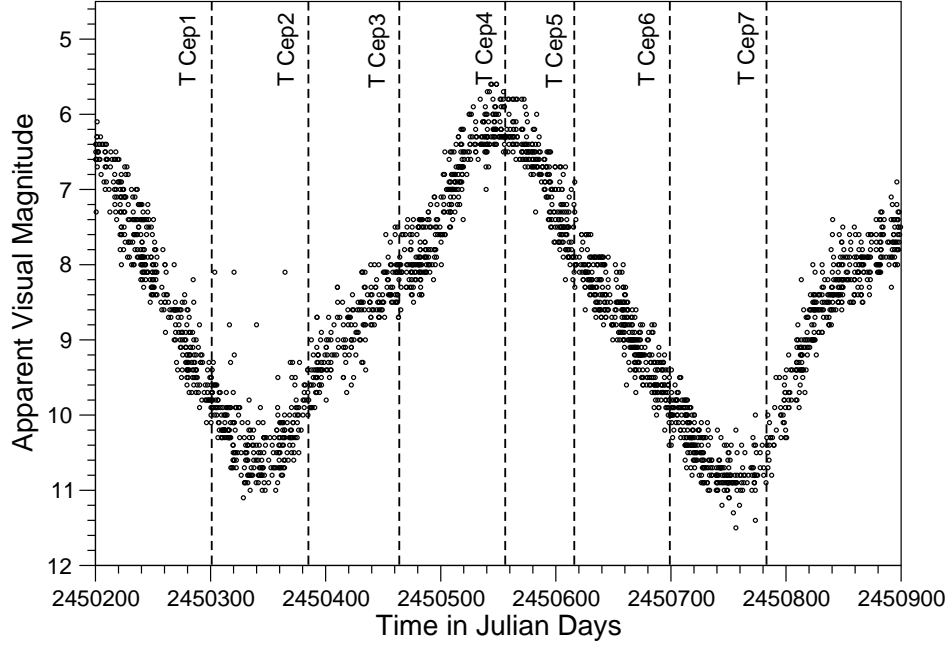


Fig. 3.— Light curve of T Cep over a 16 month period. The seven *ISO* SWS observations are indicated by dashed straight lines.

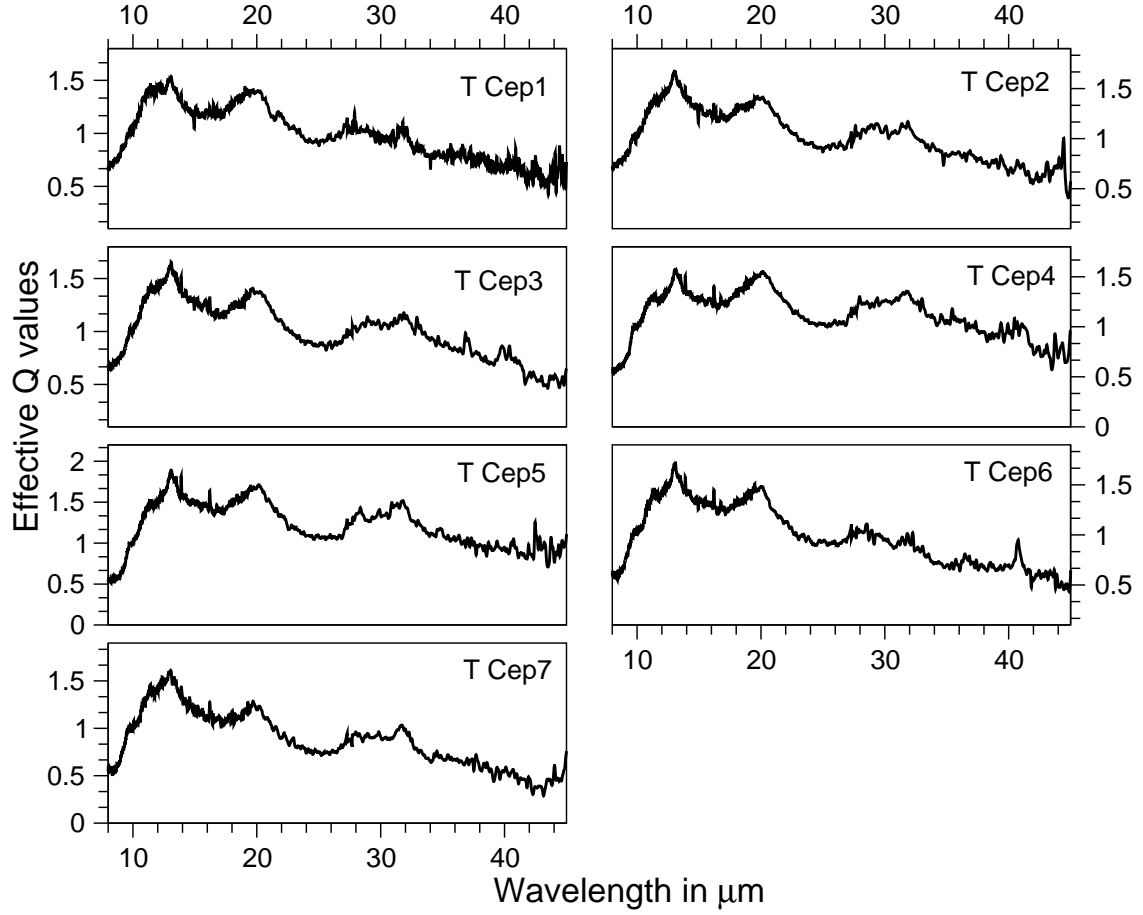


Fig. 4.— Starlight subtracted, dust-continuum-divided spectra (continuum-eliminated spectra).



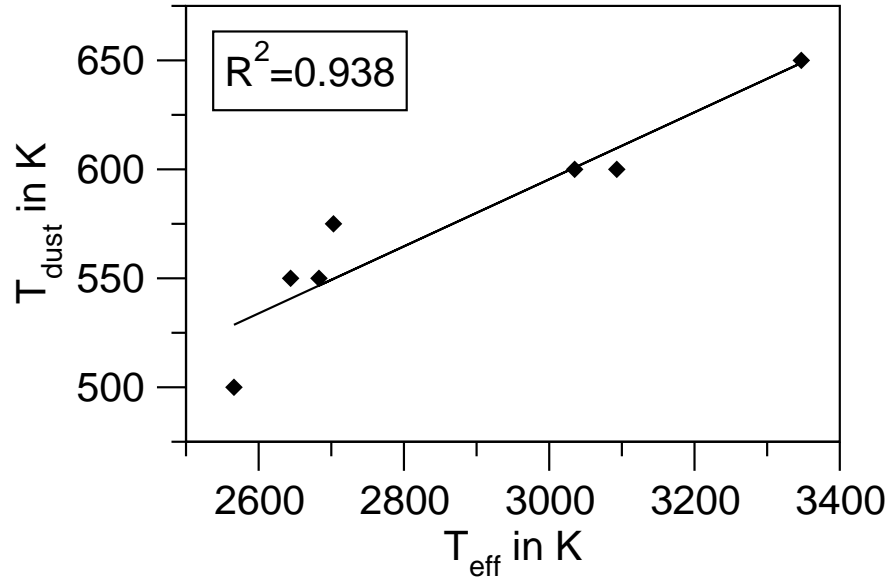


Fig. 5.— Correlation between assumed stellar temperature ( $T_{\text{eff}}$ ) and fitted inner dust temperature ( $T_{\text{dust}}$ ), along with the linear correlation coefficient.

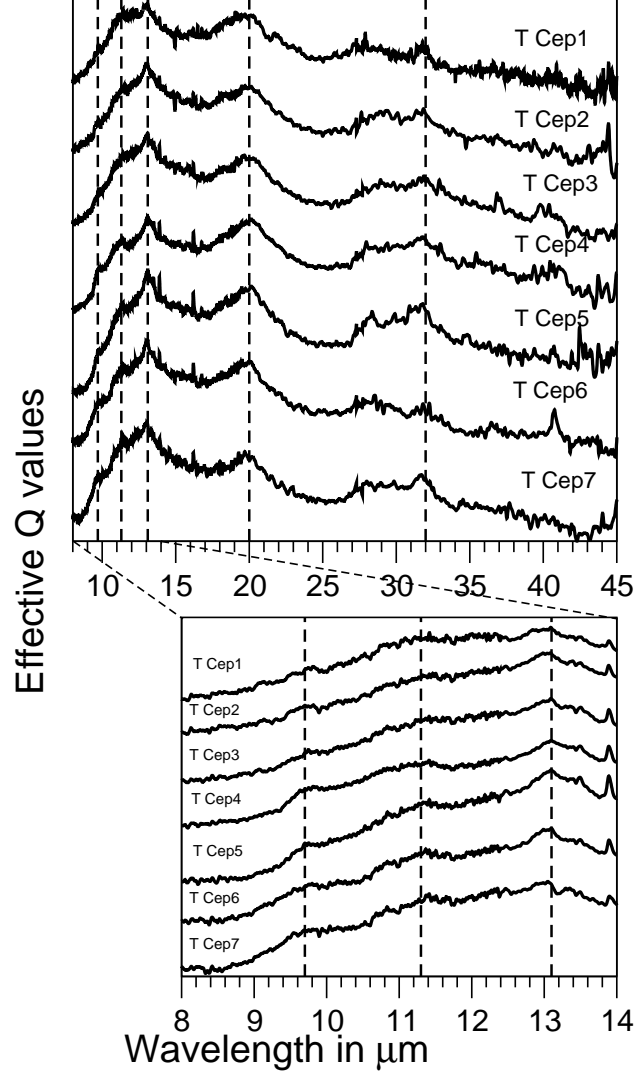


Fig. 6.— Continuum-eliminated spectra of T Cep in mid-IR region. The position of the spectral features (at 9.7, 11.3, 13.1, 20, 32  $\mu\text{m}$ ) are indicated by dashed straight lines in the top panel. The sub-peak features within the broad 8–14  $\mu\text{m}$  emission (at 9.7, 11.3, 13.1  $\mu\text{m}$ ) are explicitly shown in the bottom panel.

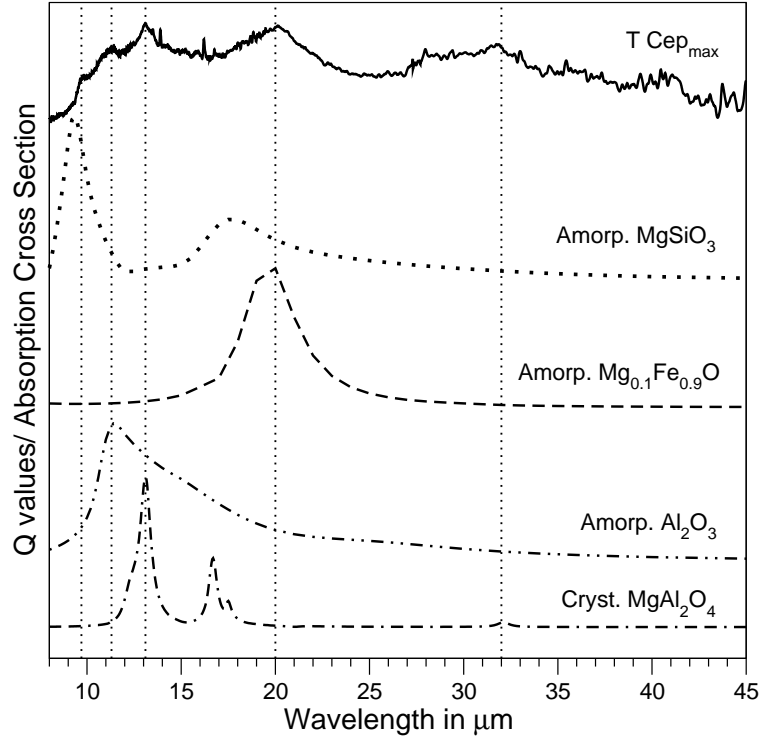


Fig. 7.— Comparison of continuum-eliminated spectra of T Cep4 (T Cep<sub>max</sub>) with several amorphous minerals suggested by Van Malderen (2003). The dotted straight lines indicate the positions of dust spectral features as shown in Figure 6.

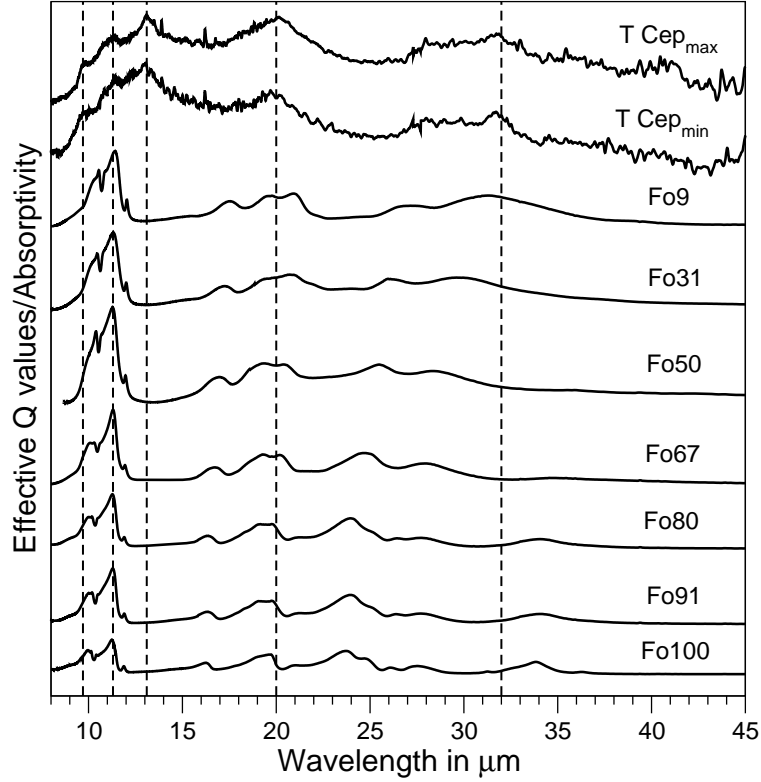


Fig. 8.— Comparison of continuum-eliminated spectra at maximum (T Cep<sub>max</sub>) and minimum (T Cep<sub>min</sub>) light with the laboratory absorptivity data for the olivine solid solution with varying Fe/(Mg+Fe) ratios. FoX (X=9, 31, 50, 67, 80, 91, 100) defines the composition such that each olivine has the composition  $\text{Mg}_{2X/100}\text{Fe}_{2-2(X/100)}\text{SiO}_4$ . The dotted straight lines indicate the positions of dust spectral features as shown in Figure 6.

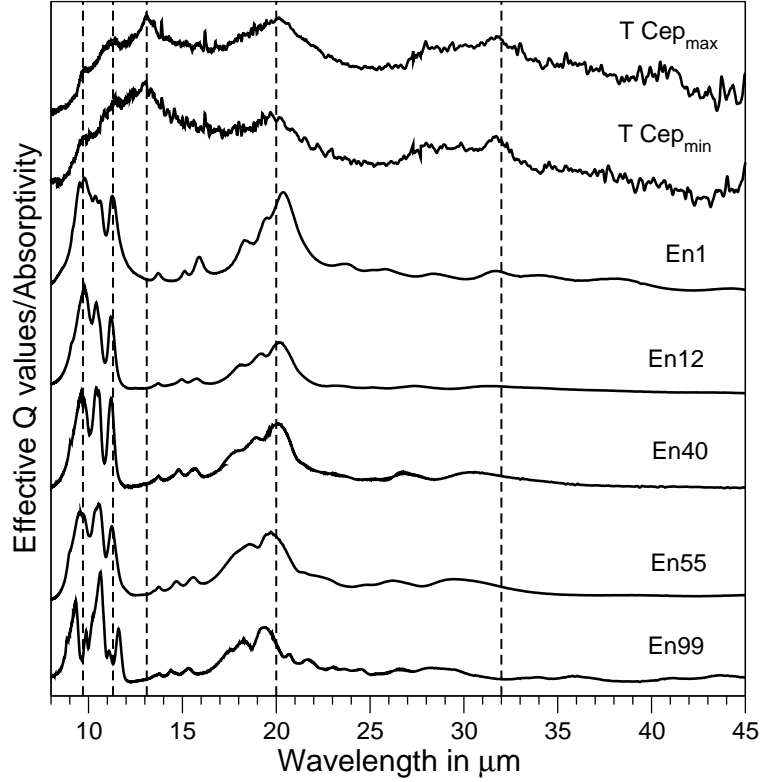


Fig. 9.— Comparison of continuum-eliminated spectra at maximum (T Cep<sub>max</sub>) and minimum (T Cep<sub>min</sub>) light with the laboratory absorptivity data for a pyroxene solid solution with varying Fe/(Mg+Fe) ratios. EnX (X=1, 12, 40, 55, 99) defines the composition such that each pyroxene has the composition Mg<sub>X/100</sub>Fe<sub>1-(X/100)</sub>SiO<sub>3</sub>. The dotted straight lines indicate the positions of dust spectra features as shown in Figure 6.

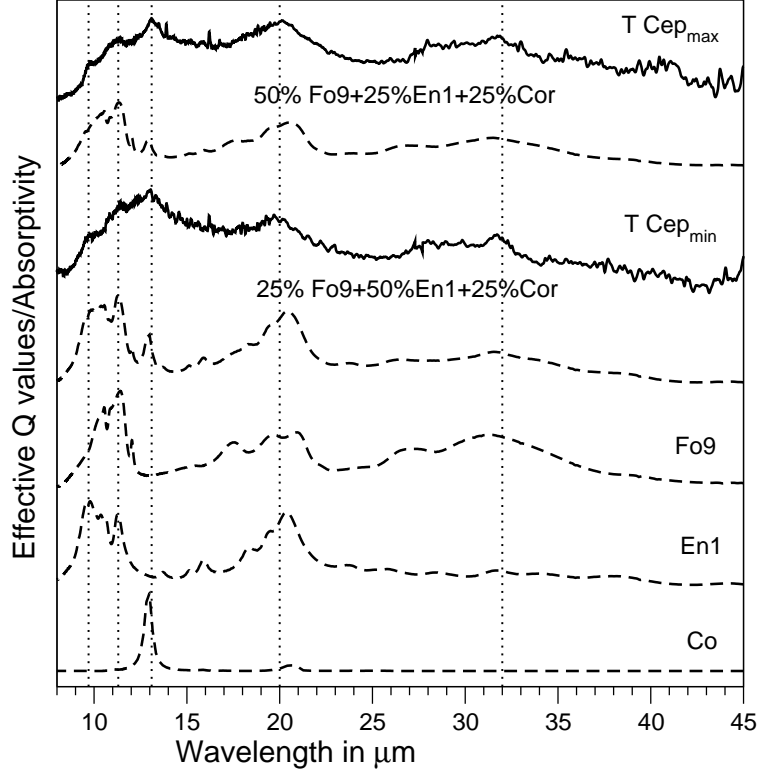


Fig. 10.— Comparisons of continuum-eliminated spectra at maximum ( $\text{T Cep}_{\text{max}}$ ) and minimum ( $\text{T Cep}_{\text{min}}$ ) light (solid lines) along with the best fit model (dashed lines) of mixtures of different potential crystalline minerals with different ratios. The laboratory data of individual crystalline minerals (Fo9, En1, Cor) are also included. The dotted straight lines indicate the positions of dust spectra features as shown in Figure 6.

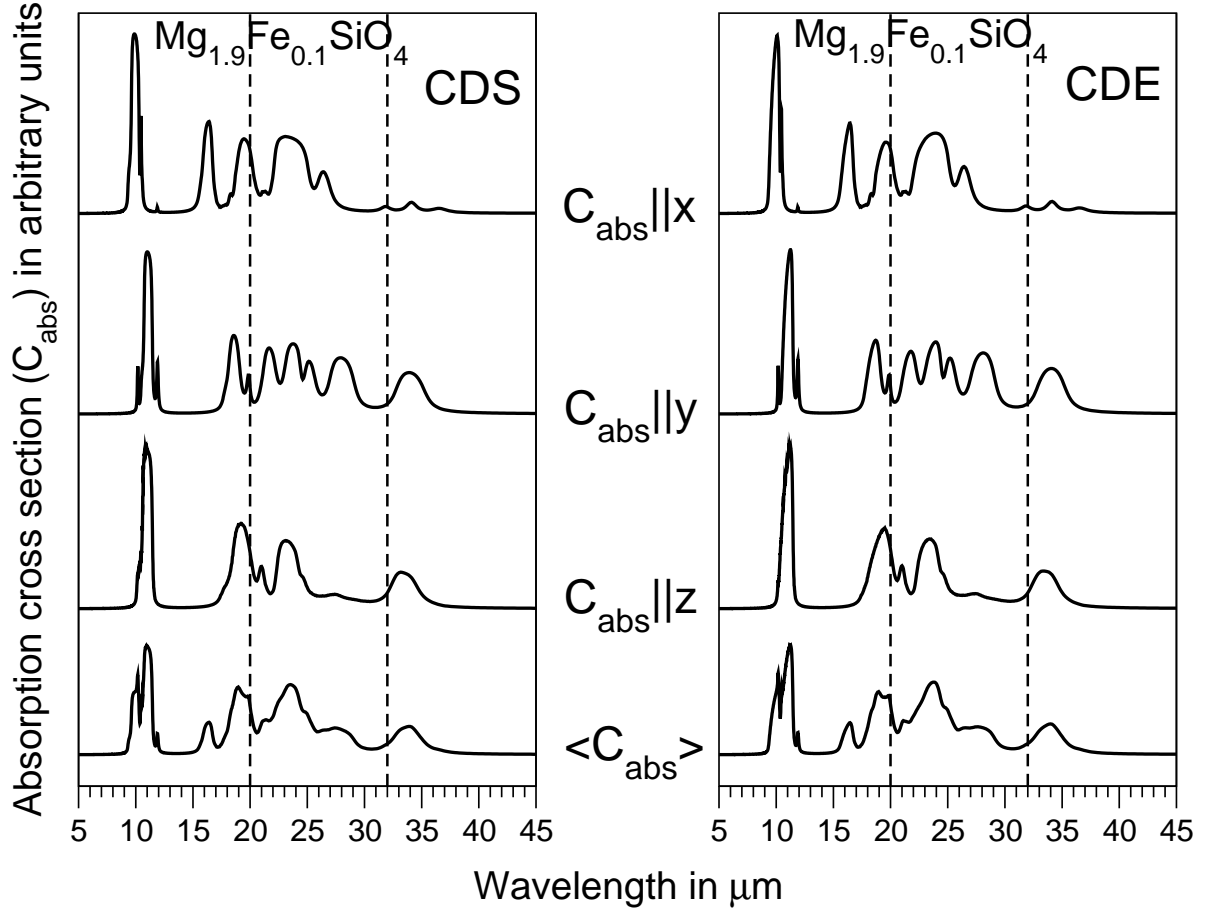


Fig. 11.— Absorption cross section of very Mg-rich Olivine ( $\text{Mg}_{1.9}\text{Fe}_{0.1}\text{SiO}_4$ ) for spheroid (CDS: left panel) and ellipsoid (CDE: right panel). The upper three plots correspond to calculated  $C_{\text{abs}}$  parallel to the  $x$ ,  $y$  and  $z$  axes. The bottom plots correspond to average ( $\langle C_{\text{abs}} \rangle$ ). Vertical dashed lines show positions of observed spectral features of T Cep at long wavelength (20 and 32  $\mu\text{m}$ ).

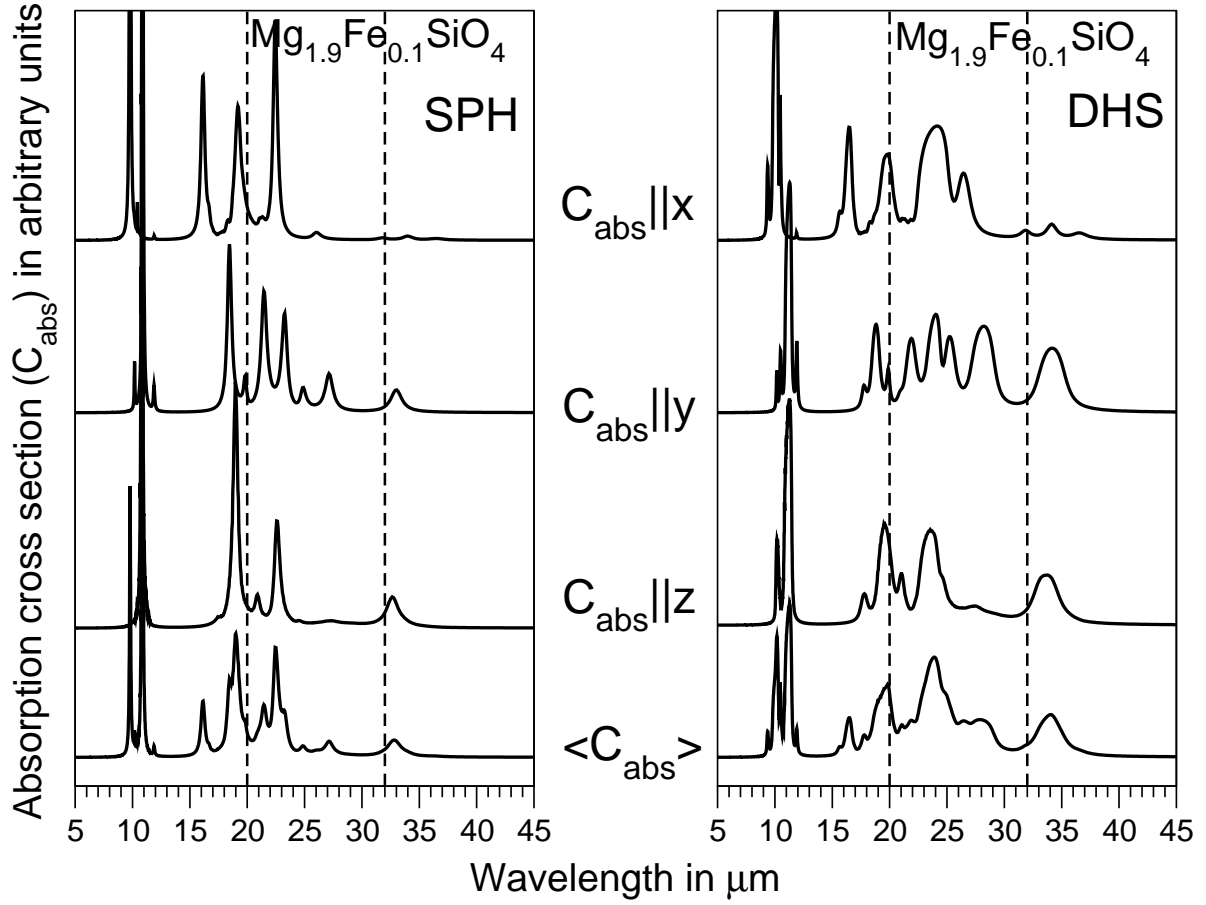


Fig. 12.— Absorption cross section of very Mg-rich Olivine ( $\text{Mg}_{1.9}\text{Fe}_{0.1}\text{SiO}_4$ ) for spherical (SPH: left panel) and hollow sphere (DHS: right panel). The upper three plots correspond to calculated  $C_{\text{abs}}$  parallel to the  $x$ ,  $y$  and  $z$  axes. The bottom plots correspond to average ( $\langle C_{\text{abs}} \rangle$ ). Vertical dashed lines show positions of observed spectral features of T Cep at long wavelength (20 and 32  $\mu\text{m}$ ).



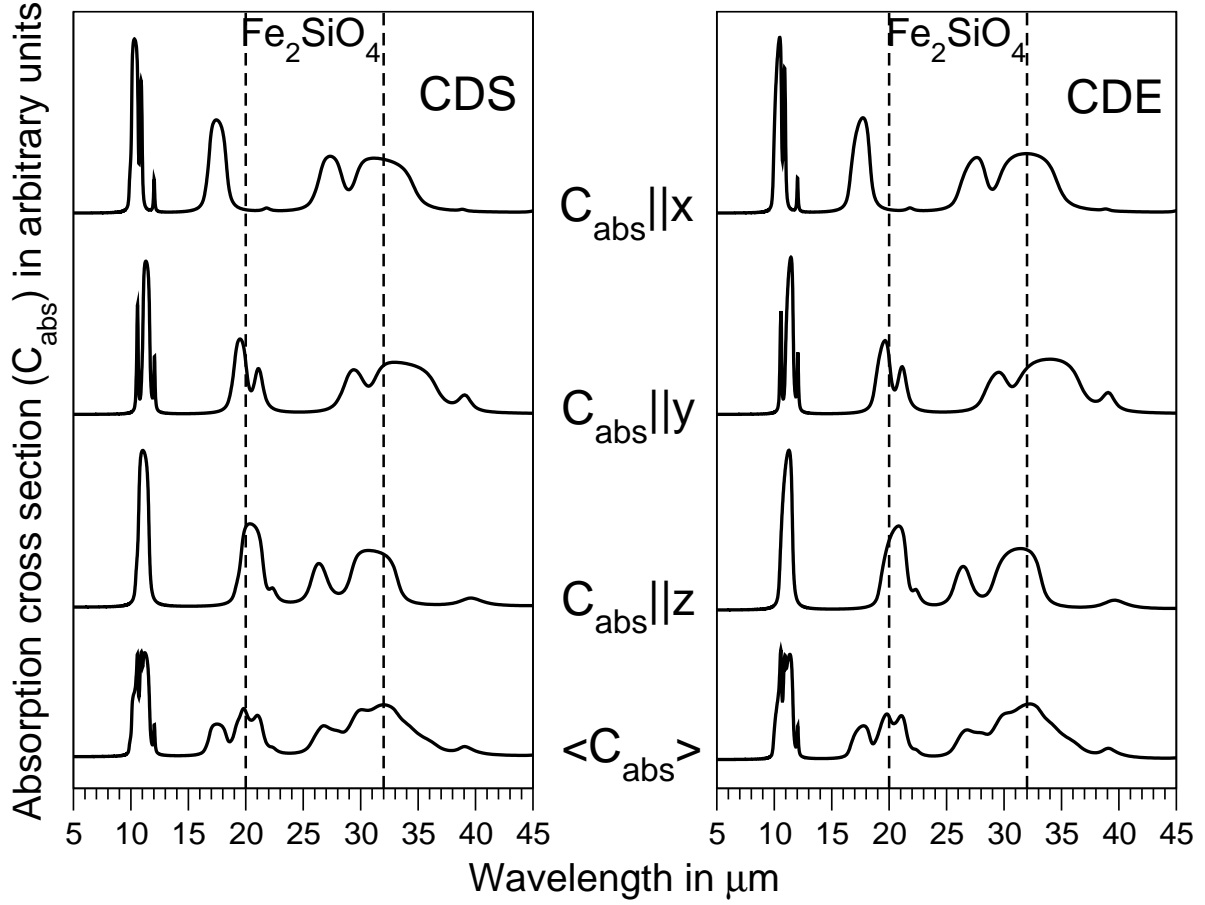


Fig. 13.— Plot of Absorption cross section of fayalite ( $\text{Fe}_2\text{SiO}_4$ ) for spheroid (CDS: left panel) and ellipsoid (CDE: right panel). The upper three plots correspond to calculated  $C_{\text{abs}}$  parallel to the  $x$ ,  $y$  and  $z$  axes. The bottom plots correspond to average ( $\langle C_{\text{abs}} \rangle$ ) of them. Vertical dashed lines show positions of observed spectral features of T Cep at long wavelength (20 and 32  $\mu\text{m}$ ).

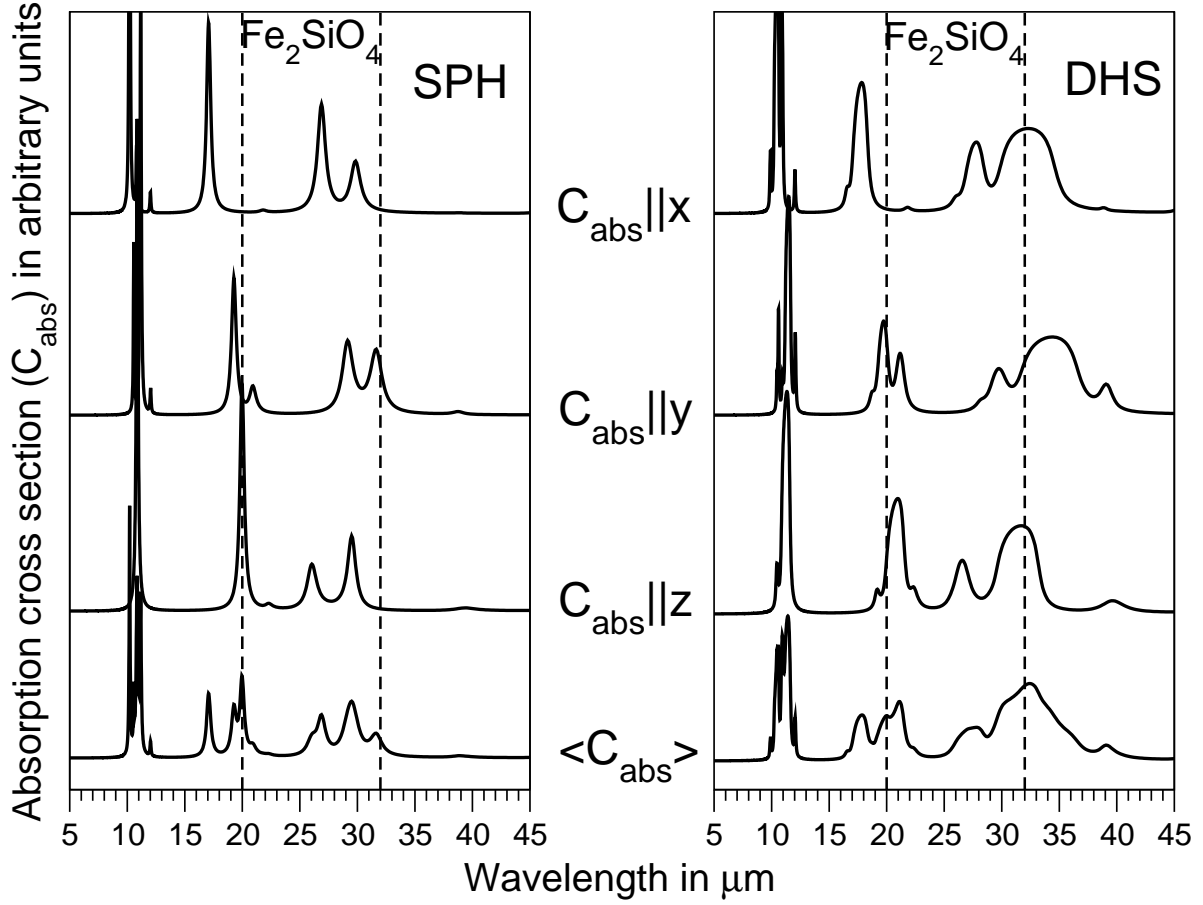


Fig. 14.— Plot of Absorption cross section of fayalite ( $\text{Fe}_2\text{SiO}_4$ ) for spherical (SPH: left panel) and hollow sphere (DHS: right panel). The upper three plots correspond to calculated  $C_{\text{abs}}$  parallel to the  $x$ ,  $y$  and  $z$  axes. The bottom plots correspond to average ( $\langle C_{\text{abs}} \rangle$ ). Vertical dashed lines show positions of observed spectral features of T Cep at long wavelength (20 and 32  $\mu\text{m}$ ).

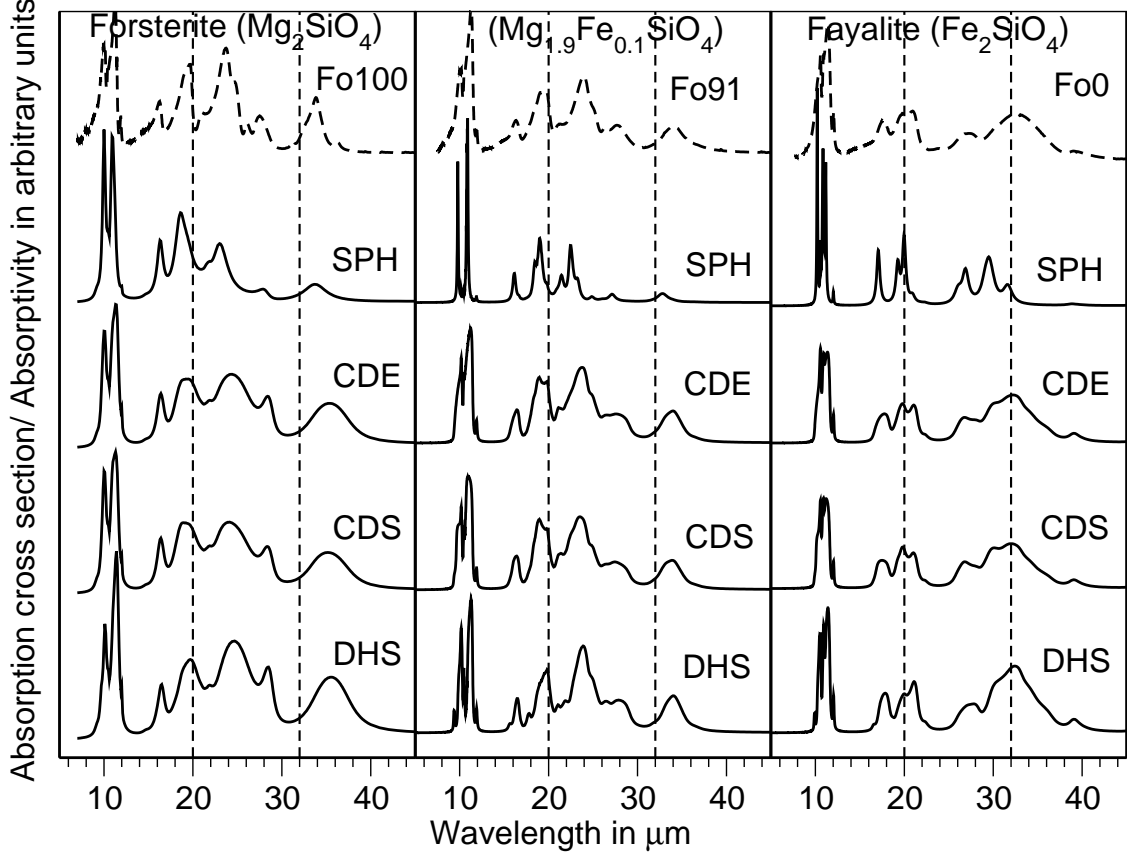


Fig. 15.— Calculated absorption cross section ( $C_{\text{abs}}$ ) for four shape distributions (SPH, CDE, CDS, DHS) of  $0.1 \mu\text{m}$ -sized grains of three different members of olivine family along with the directly-measured laboratory absorption spectrum. *Right panel:* forsterite (Fo100), *center panel:* very Mg-rich olivine (Fo91: closest compositionally in the lab spectra), *left panel:* fayalite (Fo0). Vertical dashed lines show positions of observed spectral features of T Cep at long wavelength (20 and  $32 \mu\text{m}$ ). The solid lines are the calculated absorption cross-sections while dashed lines (at the top) show the laboratory absorption spectra (data taken from Pitman et al. 2010).

Table 1: Information regarding observational data and blackbody curves.

Observation Number	TDT Number	Observation Date	Visual magnitude	$T_{\text{eff}}$ (K)	$T_{\text{dust}}$ (K)
T Cep1	26300141	08/05/1996	9.7	2703	575
T Cep2	34601646	10/27/1996	9.8	2683	550
T Cep3	42602251	01/15/1997	8.0	3035	600
T Cep4	51401256	04/13/1997	6.4	3347	650
T Cep5	57501031	06/16/1997	7.7	3093	600
T Cep6	66101436	09/07/1997	10.0	2644	550
T Cep7	74602101	12/01/1997	10.4	2566	500

Table 2: Sources of laboratory mineral data.

Sample	Chemical Composition	Designated by	Original form of lab data	References
Amorp. enstatite	MgSiO <sub>3</sub>	-	optical constants ( $n, k$ )	Jäger et al. (1994)
Amorp. alumina	Al <sub>2</sub> O <sub>3</sub>	-	optical constants ( $n, k$ )	Begemann et al. (1997)
Cryst. spinel	MgAl <sub>2</sub> O <sub>4</sub>	-	optical constants ( $n, k$ )	Fabian et al. (2001)
Amorp. Mg-Fe oxides	Mg <sub>0.1</sub> Fe <sub>0.9</sub> O	-	optical constants ( $n, k$ )	Henning et al. (1995)
Cryst. Olivine	(Mg, Fe) <sub>2</sub> SiO <sub>4</sub>	FoX	absorbance ( $a$ )	Pitman et al. (2010)
Cryst. Pyroxene	(Mg, Fe)SiO <sub>3</sub>	EnX	absorbance ( $a$ )	Hofmeister et al. in prep.
Cryst. alumina	Al <sub>2</sub> O <sub>3</sub>	Cor	optical constants ( $n, k$ )	Gervais (1991)
Cryst. Forsterite	Mg <sub>2</sub> SiO <sub>4</sub>	Fo100	optical constants ( $n, k$ )	Mukai & Koike (1990)
Cryst. Mg-rich Olivine	Mg <sub>1.9</sub> Fe <sub>0.1</sub> SiO <sub>4</sub>	Fo90	optical constants ( $n, k$ )	Fabian et al. (2001)
Cryst. Fayalite	Fe <sub>2</sub> SiO <sub>4</sub>	Fo0	optical constants ( $n, k$ )	Fabian et al. (2001)

Table 3: Correlations between flux ratios for the observed spectral features.

Continuum measured at $\rightarrow$		8.2 $\mu$ m	40 $\mu$ m
Peak Position		$R^2$	
F <sub>9.7</sub>	F <sub>11.3</sub>	<b>0.913</b>	<b>0.958</b>
F <sub>9.7</sub>	F <sub>13.1</sub>	0.489	<b>0.899</b>
F <sub>9.7</sub>	F <sub>20.0</sub>	<b>0.576</b>	<b>0.863</b>
F <sub>9.7</sub>	F <sub>32.0</sub>	0.439	<b>0.579</b>
F <sub>11.3</sub>	F <sub>13.1</sub>	0.334	<b>0.797</b>
F <sub>11.3</sub>	F <sub>20.0</sub>	<b>0.633</b>	<b>0.826</b>
F <sub>11.3</sub>	F <sub>32.0</sub>	<b>0.504</b>	<b>0.537</b>
F <sub>13.1</sub>	F <sub>20.0</sub>	<b>0.545</b>	<b>0.869</b>
F <sub>13.1</sub>	F <sub>32.0</sub>	<b>0.567</b>	<b>0.530</b>
F <sub>20.0</sub>	F <sub>32.0</sub>	0.215	0.323

Coefficients of determination ( $R^2$ )  $> 0.5$  constitutes a correlation;  
**bold** designates to which there are strong/significant correlation.